JGR Oceans

RESEARCH ARTICLE
10.1029/2020JC016580

Assessing the Impact of Nontraditional Ocean Observations for Prediction of the East Australian Current

Adil Siripatana[1], Colette Kerry[1], Moninya Roughan[1], João Marcos A. C. Souza[2], and Shane Keating[1]

[1]Coastal and Regional Oceanography Lab, School of Mathematics and Statistics, UNSW Sydney, Sydney, NSW, Australia, [2]MetOcean Division, Meteorological Service of New Zealand, Raglan, New Zealand

Key Points:

- The relative merits and trade-offs of diverse observational data streams on ocean state estimation and forecasting are assessed using two high-resolution reanalysis products of the East Australian Current (EAC) system
- A reanalysis product that assimilates all available observations better represents the ocean state compared to one that assimilates traditionally available observations only. In particular, submesoscale surface vorticity and mesoscale eddies are effectively constrained through assimilation of radar-derived nearshore surface velocities and subsurface glider observations
- In the forecast, the system that assimilates only traditionally available observations displays similar surface and subsurface predictive skill to the system assimilating all available observations

Correspondence to:

A. Siripatana and C. Kerry,
a.siripatana@unsw.edu.au
c.kerry@unsw.edu.au

Citation:

Siripatana, A., Kerry, C., Roughan, M., Souza, J. M. A. C., & Keating, S. (2020). Assessing the impact of nontraditional ocean observations for prediction of the East Australian Current. *Journal of Geophysical Research: Oceans*, *125*, e2020JC016580. https://doi.org/10.1029/2020JC016580

Received 5 JUL 2020
Accepted 17 NOV 2020

Abstract Accurate forecasting of ocean currents in dynamic regions remains a critical challenge due to the sparsity of observations in global ocean observing networks and the limited resolution of present-day regional ocean models. Lately, traditional observing platforms have been complemented by newly available data streams capable of sampling at higher spatial and/or temporal resolutions in dynamically significant regions in near-real time. However, the relative merits and trade-offs of incorporating these "nontraditional" observations into ocean state estimates have not been thoroughly investigated. Here, we perform a detailed statistical and dynamical comparison of two high-resolution reanalysis products assimilating different combinations of traditional and nontraditional observations in the East Australian Current (EAC) system, a vigorous western boundary current. We show that sea-surface height and temperature are well-constrained by satellite measurements; however, below the surface, a reanalysis incorporating fully available observations better represents the ocean state. The core of the EAC jet is effectively constrained by subsurface observations from deep water moorings upstream of jet separation, while radar-derived nearshore surface velocities in the separation zone are found to resolve the submesoscale cyclonic band inshore of the EAC. Cost function sensitivity analysis of both products reveals excessive model adjustment at depth causing the reanalyzes to overestimate alongshore transport relative to a 22-year freely evolving simulation. Overall, the assimilation of nontraditional observations delivers marked improvement in representing dynamical features of the EAC. However, this improvement is not as pronounced in the model forecast due to the introduction of nonphysical dynamics or forcing, suggesting that other improvements such as increased model resolution are required.

Plain Language Summary Estimating and forecasting the ocean state is challenging in a highly dynamic region such as a western boundary current. Integrating ocean observations with numerical models through data assimilation improves the quality of ocean prediction. This study investigates the improvement made by assimilating a range of less traditional observations (TRAD) (such as glider and high frequency coastal radar) when combined with more TRAD (such as satellite derived observations of sea surface temperature and height and deep profiles) in the East Australian Current (EAC). Overall, marked improvement in estimating the EAC dynamics has been observed when the more targeted observations are included.

1. Introduction

Both operational oceanography and ocean research applications rely critically on the combination of ocean observations from in situ and remote sensing networks with sophisticated hydrodynamic models using novel data assimilation techniques to obtain higher resolution and reduced uncertainty reanalysis products. In recent decades, significant effort in the operational oceanography research community has been directed toward improving data assimilation techniques and systems to increase the understanding and predictability of ocean currents near continental shelf regions worldwide because of their ecological and economic importance (Roughan et al., 2018). Of particular interest are western boundary currents (WBCs): warm, narrow, swift currents that flow poleward along the western side of the major ocean basins before separating from the shelf and extending eastward. WBCs and their zonal extensions strongly

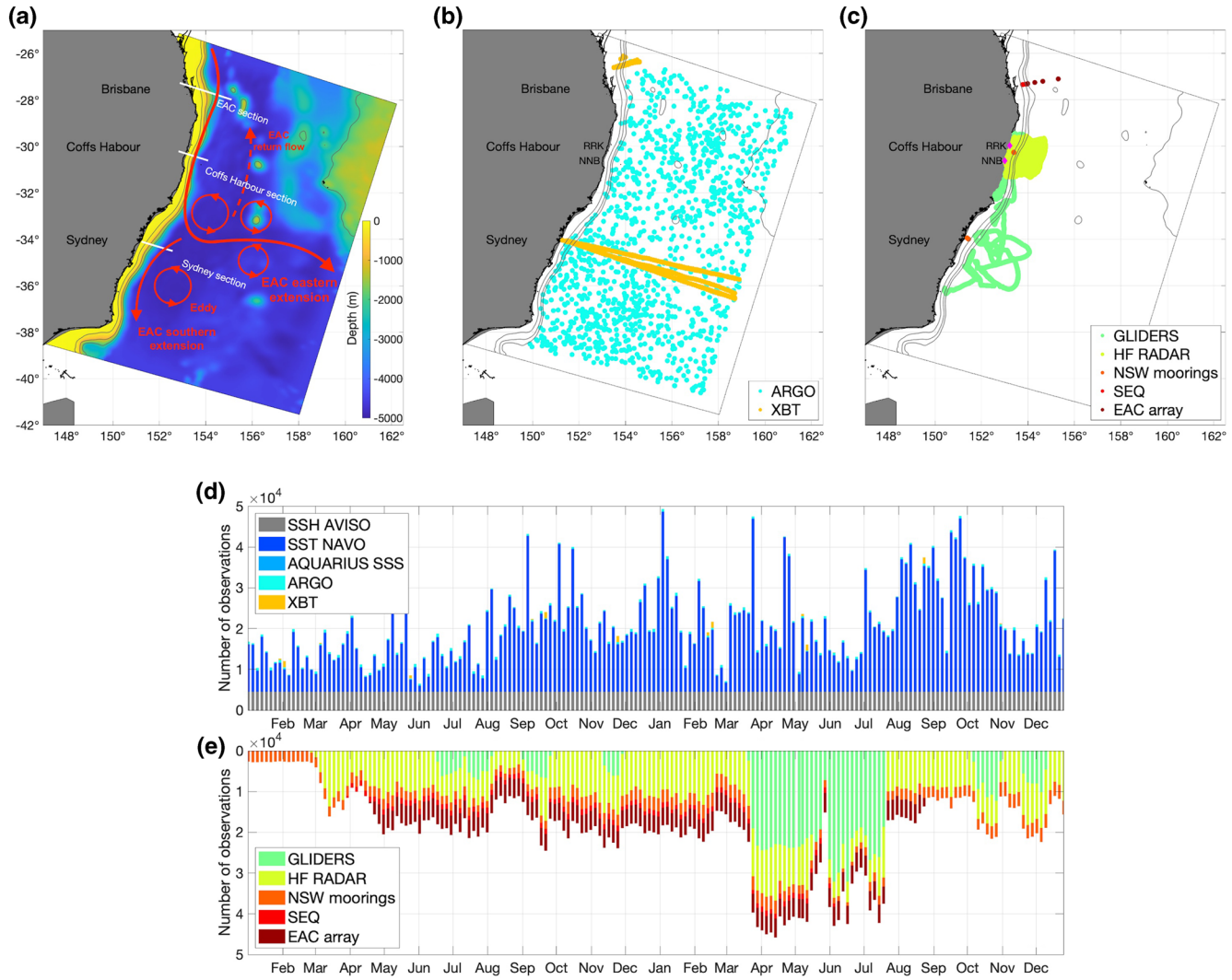

Figure 1. (a) Schematic diagram of the circulation in the EAC system. (b) Location of traditional observations used in the TRAD assimilation (SSH, SST, and sea surface salinity are not shown). (c) Location of additional observations used in the FULL assimilation. (d) Number of observations from each traditional observation platform in each 5-day assimilation window over the 2-year reanalysis. (e) Number of observations from each observation platform in each 5-day TRAD assimilation window over the 2-year reanalysis. The gray contour lines off the coast in panels (a–c) are 200-, 1,000-, and 2,000-m isobaths, respectively. EAC, East Australian Current; SSH, sea surface height; SST, sea surface temperature; TRAD, traditional observations.

influence regional shelf circulation, coastal ecology (Lee et al., 1981; Shulzitski et al., 2015), and fisheries (Richardson et al., 2009). WBC systems are highly dynamic and are associated with flow instability, abundant mesoscale variability and high kinetic energy (Mata et al., 2000; Stammer, 1997), which make them challenging to monitor (Feron, 1995; Imawaki et al., 2013; Roughan et al., 2014, 2017) and forecast (Metzger et al., 2014).

The East Australian Current (EAC) is the WBC for the South Pacific subtropical gyre (Figure 1a). The EAC flows southward along the southeastern coast of Australia and intensifies at around 31° S (Kerry & Roughan, 2020a) as the continental shelf reaches its narrowest point (16 km) before separating from the coast between 31°S and 32.5°S (Cetina Heredia et al., 2014). The zonal extension of the EAC turns eastward to form the EAC eastern extension, shedding large warm core eddies in the Tasman Sea (Cetina Heredia et al., 2014; Oke & Middleton, 2000). Despite having the weakest mean flow among the WBCs (Mata et al., 2000), the EAC has high-eddy variability (Mata et al., 2006). The EAC southern

extension is a complex region where eddy dipoles can drive cross-shelf exchange (Malan et al. 2020; Ribbat et al., 2020).

Among the first data assimilating efforts to understand the EAC circulation (e.g., Oke et al., 2013; Sakov & Sandery, 2015), Zavala-Garay et al. (2012) and Kerry et al. (2016) are considered the first to utilize the combined Regional Ocean Modeling System (ROMS) and 4-dimensional variational (4D-Var) data assimilation scheme in the region. Variational data assimilation techniques solve for the analysis through an optimization framework using variational calculus to provide the "best" estimate of the ocean state given the available observations and underlying dynamical model (Le Dimet & Talagrand, 1986; Lewis & Derber, 1985). Incremental Strong-constraint 4D-Var (IS-4DVAR), in particular, solves for the increments in the initial condition, model forcing, and boundary conditions such that the distance between the revised model trajectory and all the observations in a specific time window is minimized in a least-square sense and assumes a perfect model. The technique makes use of the tangent linear model to iteratively update the model increments in the cost function minimization process within each assimilation window (Di Lorenzo et al., 2007).

Zavala-Garay et al. (2012) assimilated data from traditional ocean observing platforms (i.e., satellite-derived sea surface height (SSH) and temperature, and vertical temperature profiles from expandable bathythermographs) into a coarse-resolution model of the EAC (18–30 km horizontal grid) to evaluate the skill of the reanalysis to predict mesoscale variability of the EAC for 2001–2002. By introducing additional subsurface pseudo-observations based on an empirical relationship between surface observations and subsurface variability, the forecast skill of their (low resolution) system was found to be reliable for up to 2 weeks for the upper 1,000 m of the ocean.

In contrast to Zavala-Garay et al. (2012), which relies upon traditional observational data streams, Kerry et al. (2016, 2020a) developed a reanalysis of the EAC assimilating newly available observations derived from high-frequency (HF) radar, shelf moorings, gliders, and a full transport resolving mooring array together with the range of preexisting traditional observational platforms to yield the "best estimate" of the ocean state in the EAC area over the assimilation period, 2012–2013. Kerry et al. (2016) used ROMS, the ROMS (Shchepetkin & McWilliams, 2005) and the IS-4DVAR data assimilation scheme (Moore et al., 2011) with a horizontal gridscale of 2.5 km (over the shelf) to 6 km (in the open ocean) and 5 km in the along shore direction.

Kerry et al. (2018) used the reanalysis from Kerry et al. (2016) to assess observation impact in the EAC and found that observations taken in regions of greater dynamical variability have the strongest influence on the circulation estimates. Large data volume and dependency between each data stream was also shown to be a dominant factor in determining the impact of the observations on the model adjustment. For instance, large volumes of satellite sea surface temperature (SST) data with long decorrelation length-scales have the greatest total impact but small impact per observation. Kerry et al. (2018) also found that observations situated in the EAC jet such as moorings and HF radar can propagate information away from the observation site.

In operational oceanography where the emphasis is on real-time forecasts, the assimilation framework is generally limited to what we refer to as "traditional" observations such as satellite-derived measurements and vertical profiles from ARGO floats that historically were the only datasets available in real-time. The merits and trade-offs of assimilating observations from more modern observational platforms such as HF radar, gliders and deepwater and shelf moorings and the impact of these observations on the representation of the EAC dynamics by the reanalysis have yet to be thoroughly investigated. In this study, we seek to assess a reanalysis product utilizing the full suite of all available observations (hereafter referred to as FULL) with a reanalysis product that only assimilates traditionally available operational data streams (TRAD). As a control and benchmark, we also examine a 22-year nonassimilating freely evolving simulation (Kerry & Roughan 2020b). We first investigate the ability of the two reanalyzes (TRAD and FULL) to represent assimilated and nonassimilated observations using a range of statistical analyses. Dynamical distinctions between the two models are explored by looking at features such as volume transport, core structure, and surface vorticity. The cost function sensitivities that describe the propagation of the assimilated information are assessed and discussed to explain the results. Finally, we examine the temporal evolution of surface and subsurface variables to compare the predictive skills of the two models.

Table 1
Description of the Model Runs Used (Reanalyses and Free-Running); Showing Case Name, the Data They Assimilate, the Time Period and the Papers Describing the Cases and the Data Citations

Case	Assimilated data	Time period	Model description and data citation
Traditional observations (TRAD)	SSH, SST, SSS Argo floats and XBTs	January 12–December 13	-
Fully available observations (FULL)	TRAD + HF radar, moorings and gliders	January 12–December 13	Kerry et al. (2016, 2020a)
2-year free-running model (FREE)	-	January 12–December 13	Kerry et al. (2016)
22-year free-running model (FREE22)	-	January 94–September 16	Kerry and Roughan (2020a, 2020b)

Abbreviations: HF, high frequency; SSH, sea surface height; SSS, sea surface salinity; SST, sea surface temperature; XBTs, expendable bathythermographs.

FULL: This refers to the reanalysis product that assimilates all available observations (SSH, SST, SSS, Argo, XBT, HR radar, shelf and deep moorings and glider data: see Section2.3) over the 2-year period from January 2012 to December 2013. It is the same as the system described in detail in Kerry et al. (2016, 2020a) except for the modifications described below.

TRAD: This refers to the reanalysis product that is identical to FULL in its data assimilation configuration, expect that it only assimilates "traditionally available" observations (SSH, SST, SSS, Argo, and XBT: see Section 2.3).

FREE: This refers to the free-running (nonassimilating) simulation over the 2-year period from January 2012 to December 2013. It is used to show the improvement gained by assimilating observations (FULL and TRAD) over the 2-year period (e.g., in Figures 3–5 of this study and in Figures 9–15 of Kerry et al. [2016]).

FREE22: This refers to the free-running simulation over a 22-year time period from January 1994 to September 2016, described in Kerry and Roughan (2020a, 2020b).

2. Model Configuration

2.1. The ROMS Configuration

In this study, we adopt the model configuration of the EAC system described in Kerry et al. (2016, 2018, 2020b). The model uses the ROMS to simulate the mesoscale eddy-dominated ocean circulation off the southeastern coast of Australia. ROMS is a free-surface, hydrostatic, primitive equation ocean model widely used in the oceanography research community (Haidvogel et al., 2000; Marchesiello & Middleton, 2000; Shchepetkin & McWilliams, 2005). The hydrostatic primitive equations in ROMS are solved on a curvilinear grid with a terrain following vertical coordinate system.

The study domain extends along SE Australia from 25.25° S to 41.55° S and roughly 1,000 km offshore (Figure 1a). This domain is chosen such that it covers the area of maximum EAC jet coherence, the EAC separation region, the region of high eddy activity associated with the EAC eastern extension, and the EAC southern extension. The grid is rotated 20° clockwise such that the coastline is oriented roughly parallel with the domain's *y*-axis. The cross-shore horizontal resolution varies from 1/44° (2.5 km) over the continental shelf to resolve the shelf at the narrowest point (31°S) and gradually increases to 1/18° (6 km) offshore. The horizontal resolution is 1/22° (5 km) in the along-shore direction. The EAC shelf is narrower than most WBC shelves ranging 16–30 km upstream of its separation (Roughan & Middleton, 2002, 2004), so care was taken when developing the grid to maintain the shelf width. High resolution over the shelf helps minimize pressure gradient errors that emerge in terrain following coordinate schemes, which otherwise may result in artificial along-slope flow for steep topography (Haney, 1991; Mellor et al., 1994). Topographic smoothing is applied to the model to ensure low horizontal pressure gradient errors while still representing the shelf and seamount structures. The model utilizes 30 vertical S-layers with higher resolution in the upper 500 m to resolve mesoscale dynamics and higher resolution near the seabed for improved accuracy at the bottom boundary layer. To better resolve surface currents, a near-constant-depth surface layer is provided by applying the vertical stretching scheme of De Souza et al. (2015). Initial conditions and boundary forcing are derived from the Bluelink ReANalysis version 3p5 (BRAN3p5; Oke et al., 2008, 2013). The model bathymetry at all three open boundaries is merged to the BRAN3 bathymetry. Any misfits in baroclinic energy to the BRAN3 condition are absorbed at the boundary via a flow-relaxation scheme.

In this study we refer to four different configurations of the EAC ROMS model. Each case is described below and summarized in Table 1, also see Section 2.3.

The FULL, TRAD, and FREE configurations are forced at the surface with 6-hourly atmospheric fields provided by the 12 km resolution Bureau of Meteorology (BOM) Australian Community Climate and

Earth-System Simulation (ACCESS) reanalysis (Puri et al., 2013). Adjustments made compared to the configuration of Kerry et al. (2016) are (1) The upper ocean temperature (warm) bias was improved in the free-running configuration by scaling the air temperature in the atmospheric forcing to better match other atmospheric products. (2) We removed daytime SST observations and any night observations when the wind speed was less than 2 m/s to account for skin temperature effects. The percentage of SST observations removed per 5-day cycle is 0.33%–54.3% (mean of 20.77%). (3) The observation errors applied to the temperature profiles from the expendable bathythermographs (XBTs) were doubled to better account for the uncertainty in the timing and location of the XBT measurements. (4) The temperature vertical decorrelation scale was relaxed to 20 m (from 10 m) to improve the projection of SST observations to the subsurface. Overall these changes resulted in smaller initial cost functions and smaller differences between the final nonlinear the final tangent-linear cost functions, indicating a more stable reanalysis system.

The FREE22 surface forcing is provided by daily atmospheric fields from the National Center for Environmental Prediction's (NCEP) reanalysis atmospheric models (Kistler et al., 2001). FREE22 has been found to represent well the mean flow, seasonal, and intra-annual variability of the EAC. This study uses FREE22 for the purpose of benchmarking the representation of the EAC dynamics by the FULL and TRAD reanalyses/forecasts.

2.2. The 4D-Var Assimilation Configuration

4D-Var solves for increments in model initial conditions, boundary conditions, and forcing in such a way that the model trajectory over a specific assimilation window is optimized by minimizing the cost function involving the background, the observations, and their associated error covariances in a least-squares sense.

Assuming Gaussian errors for observations and model prior, the gradient of the cost function we seek to minimize is of the form

$$\nabla_{\delta z}\boldsymbol{J} = \sum_{i=0}^{n} \boldsymbol{M}\left(t_i,t_0\right)^T \boldsymbol{H}_i^T \boldsymbol{R}_i^{-1}\left(\boldsymbol{H}_i \boldsymbol{M}\left(t_i,t_0\right)\delta z - \boldsymbol{d}_i\right) + \boldsymbol{P}^{-1}\left(\delta z\right), \tag{1}$$

where δz is the augmented vector of the model's initial conditions, surface forcing and boundary conditions from time step t_1 to t_n with T denotes the transpose. $\boldsymbol{M}\left(t_i,t_0\right)^T$ is the adjoint of the tangent linear model which integrate the model back in time. $\boldsymbol{H}_i$ represents the nonlinear observation operator mapping the model values to the observations space. The difference between the background and the observations at time i is computed in the innovation $\boldsymbol{d}_i = \boldsymbol{y}_i - \boldsymbol{H}_i\left(\boldsymbol{x}^b\left(t_i\right)\right)$, where $\boldsymbol{y}_i$ is the observations vector. The uncertainty of the observations and the model background is defined in the observation error covariance matrix $\boldsymbol{R}$ and the background error covariance matrix $\boldsymbol{P}$, respectively.

The ROMS framework used in this study has a suite of tools including a tangent linear version of the nonlinear model and its associated adjoint operator, tailor-made to solve 4D-Var optimization problems for large-scale coastal/regional ocean system. The tangent linear and adjoint components of ROMS were introduced by Moore et al. (2004).

The IS-4DVAR configuration for the FULL case is described in detail in Kerry et al. (2016). We adopt the same configuration to build the TRAD reanalysis (traditional observations only); the only difference is the smaller number of observations assimilated. A 5-day assimilation window was employed as the tangent linear model assumption remains valid over this time period.

2.3. Observations: The Two Reanalysis Products

The two reanalysis products used in this study assimilate different combinations of what we refer to as traditional and nontraditional observations. The TRAD reanalysis includes the assimilation of readily available operational observations including satellite-derived SSH, SST, sea surface salinity (SSS), vertical profiles of temperature and salinity from profiling Argo floats and vertical profiles of temperature from XBTs. The FULL product includes the TRAD observations, as well as surface velocity measurements from HF coastal

radar (HF radar), temperature and velocity observations from continental shelf moorings off the coast of New South Wales (NSW) and Southeast Queensland (SEQ), data from five deep water moorings in the EAC transport array, and ocean gliders. The locations and volume of the observations over the 2-year simulation period are shown in Figure 1. The reader may refer to Kerry et al. (2016) for more detailed specifications of the above-mentioned data, the processing performed prior to assimilation and the prescribed observation uncertainties.

3. Results

3.1. Representation of Observations

In this section, we assess the performance of the two systems (FULL and TRAD) in analysis mode to represent both assimilated and nonassimilated observations. First, the representation of the traditional observations in both systems is analyzed. Then the representation of the nontraditional observations by both the FULL case (in which they are assimilated) and the TRAD case (in which they are not assimilated) is compared. Finally, assessment of the representation of conductivity–temperature–depth (CTD) cast observations not assimilated into either system is performed.

3.1.1. Traditional Observations

3.1.1.1. Sea-Surface Height

The skill of the FULL and TRAD reanalysis in representing SSH observations was evaluated using the root mean square (RMS) observation anomaly with respect to the time mean, and the RMS difference between the reanalyzes and observations (Figure 2). The observed SSH exhibits greater variability than the two reanalyzes, as is evident from the maximum in RMS anomaly around 33°S. However, both FULL and TRAD reanalyzes successfully represent the overall structure of the SSH variability, with a maximum RMS anomaly of approximately 0.35 m located at around the same latitude.

The time series of spatially averaged RMS SSH observation anomaly and RMS SSH difference between the FREE, FULL, and TRAD cases and the observations are depicted in Figure 2a. Each point in the series represents a single assimilation window. The RMS difference for both TRAD and FULL cases are similar in magnitude and notably smaller than the RMS anomaly of the observations and the free-run. The time series further emphasizes the better performance of the TRAD reanalysis compared to the FULL reanalysis, with the 2-year time mean of RMS SSH difference being lower (0.06 m) for TRAD compared to the FULL (0.075 m).

The RMS difference between the analyses and observations for the TRAD and FULL cases is small compared with the variability of the observations (Figures 2c and 2e), with FULL showing slightly greater spatial mean RMS difference (0.075 m) than the TRAD case (0.059 m). This indicates better performance for TRAD in representing the SSH observations, an expected result because the TRAD assimilation is not constrained by other observations present in the FULL assimilation system.

3.1.1.2. SST and Subsurface Temperature

A clear improvement of FULL and TRAD cases in matching the SST observations compared to the free run is shown in Figure 3a. The time mean RMS SST between observations and the FREE is at 1.26°C; larger than those of the reanalyzes. Similar to the results obtained for SSH, the SST errors for the FULL case is slightly larger than those of the TRAD case, with the time mean of 0.39°C for FULL and 0.36°C for TRAD. This effect is again caused by the FULL case trying to fit other nontraditional observations omitted from the TRAD reanalysis.

Figures 3b and 3c show the RMS difference of subsurface temperature between models (FREE, FULL, and TRAD) and observations from ARGO and XBT profiles, respectively. Overall, we observe a marked improvement of the reanalyzes in estimating the subsurface temperature of the upper 1,000 m with respect to the FREE, with both FULL and TRAD analysis RMS difference reduced to a range of 0.7–1°C

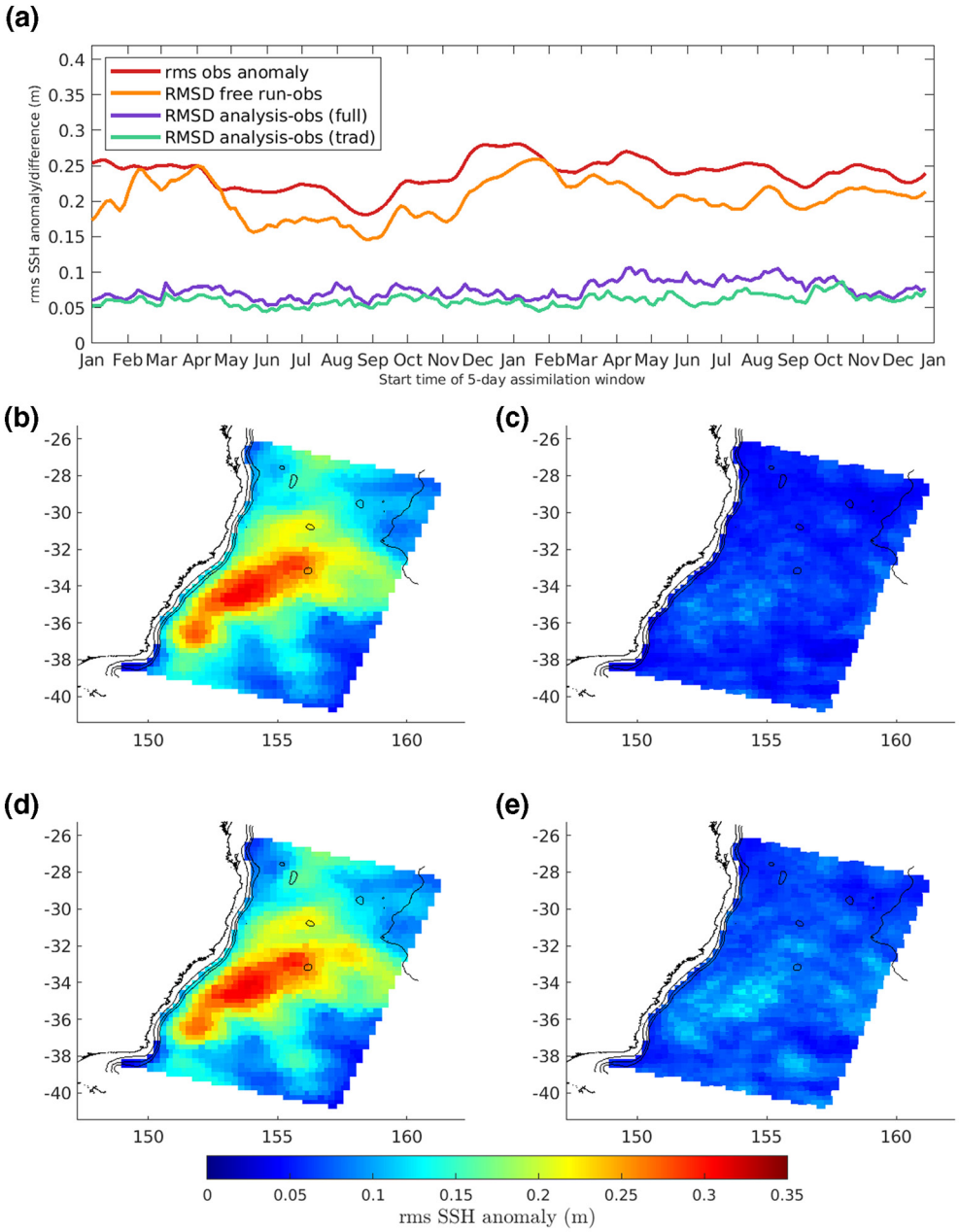

Figure 2. (a) Timeseries of the root mean square (RMS) SSH difference between the analysis and observations, both for FULL and traditional observations (TRAD), for each assimilation window. RMS sea surface height (SSH) anomaly over 2-year period from (b) TRAD analysis, and (d) FULL analysis. RMS SSH difference between (c) TRAD case and observations and (e) FULL case and observations.

from the free run value of around 1.9°C for ARGO, and reduced to a range of 0.5–1.1°C from the maximum free run value around 2.7°C for XBT observations in the upper 500-m depth. Below 500 m, the observations are sparse in both time and space and the circulation is less influenced by the mesoscale circulation, which results in smaller differences between the two analyses and the free-running simulation below such depth. For ARGO floats in which the observations have good spatial and temporal coverage over the 2-year period, the TRAD case gives slightly lower RMS difference both in the analysis and forecast compared to the FULL case across the upper 500-m depth. This is also to be expected as the FULL case is fitting other surface observations.

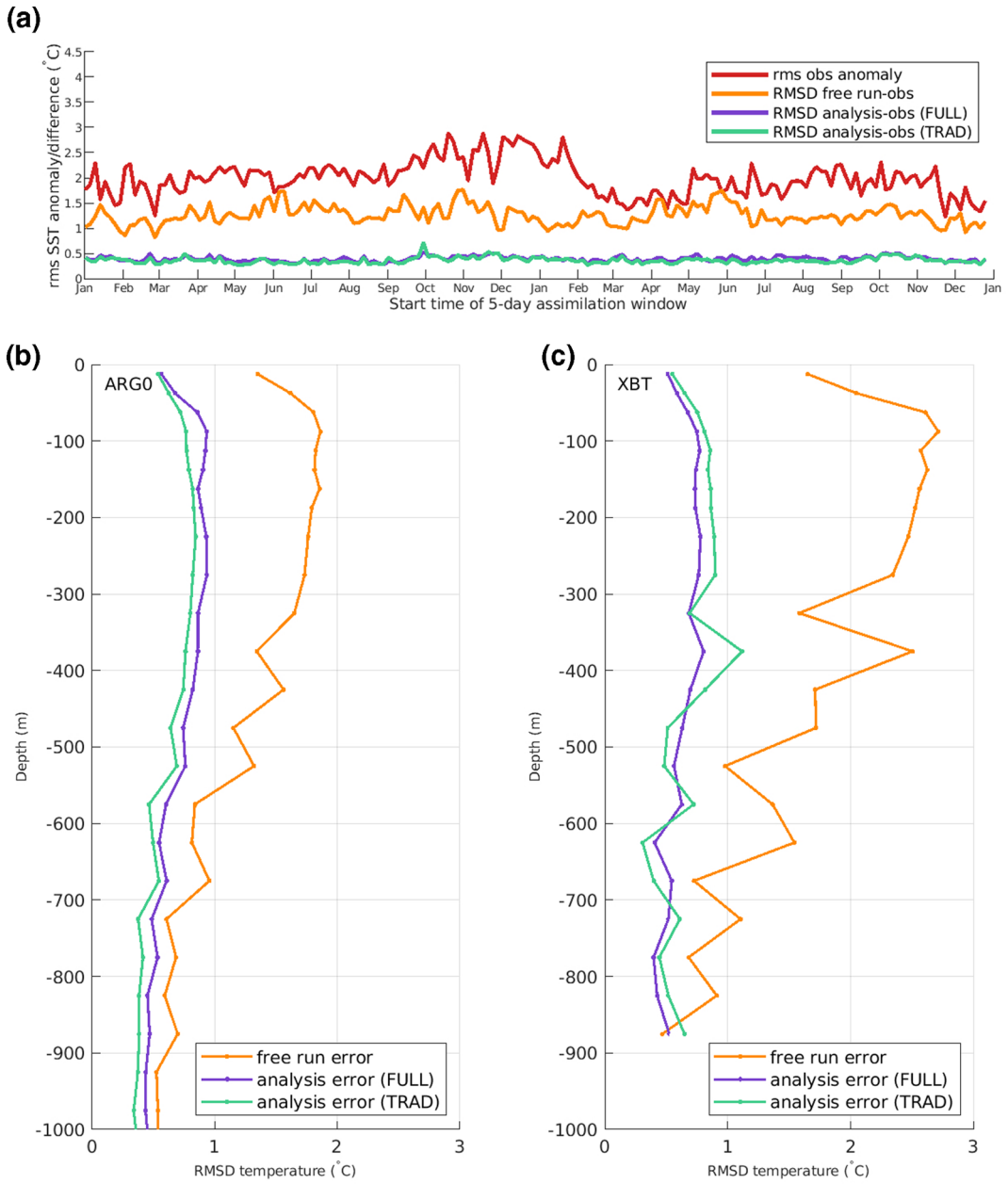

Figure 3. (a) The RMS difference in sea-surface temperature between the analysis and observations the for FULL and TRAD cases, for each assimilation window. Profiles of RMS temperature difference between the free run and observations, the analysis (FULL and TRAD) and observations for (b) Argo subsurface temperature profiles, averaged over the 2-year assimilation period, and (c) as in (b) for XBT subsurface temperature profiles. Argo and XBT depth bins are 25 m from the surface to 200 and 50 m below 200 m. RMS, root mean square; TRAD, traditional observations; XBT, expendable bathythermograph.

3.1.2. Nontraditional Observations

3.1.2.1. Surface Currents From HF Radar

For the representation of the nontraditional observations by the two models, we first examine their estimates of surface currents under the radar footprints. The scalar radial current speeds as measured by two radar sites are converted into surface velocities and compared with the surface velocity outputs from the FULL and TRAD cases. We use complex correlations between the observations and FULL and TRAD as a

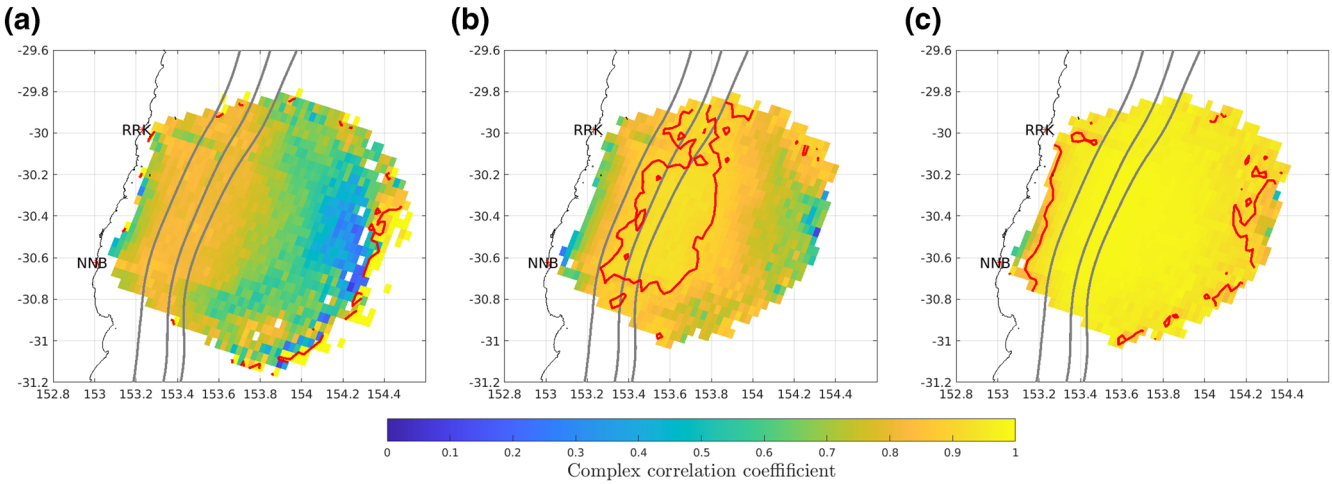

Figure 4. (a) Complex correlation of surface velocities computed from the assimilated high-frequency radar radials, and surface velocities computed from the FREE, (b) TRAD analysis, and (c) FULL analysis. 200-, 1,000-, and 2,000-m bathymetry contours are shown using gray lines. Red lines show the 0.9 complex correlation contour. TRAD, traditional observations.

measure of similarity between each velocity field. Note that this comparison is available only at the location where the radar beams from two sites overlaps. Also, for computation, we only include the grid cells where the beam intersection angle is greater than 30°, in which the conversion of radial speed to velocity components are considered accurate (Kerry et al., 2016).

The complex correlations between the observed and modelled surface velocities are shown in Figure 4. The complex correlation of surface velocities between FREE and the observations exhibits values of 0.75–0.9 over the EAC core and lower values offshore of the continental shelf slope where the circulation is more eddy-dominated. There is considerable improvement in complex correlations for the TRAD analysis compared to the FREE, with the region over the EAC core exhibiting complex correlations larger than 0.9, with lower correlations in- and off-shore. For the FULL analysis, the surface velocity is well represented across the HF radar footprint with the majority of the observed area having a complex correlation greater than 0.9, except around the edge of the coverage region where there are few observations or the radial speeds are small.

3.1.2.2. Moorings

To compare the performance of the FULL and TRAD cases in reproducing subsurface velocities we investigate the complex correlation between velocity observations (from moored ADCPs) and modeled velocities for several profiles (Figure 5). The mean complex correlation across the depths for the FULL analysis are 0.91 ± 0.08 and 0.94 ± 0.06 for the SEQ200 and SEQ400, respectively. These moorings are located on the shelf and shelf-slope at the latitude where the EAC is found to be most coherent. The corresponding TRAD analysis complex correlations are considerable better than the FREE throughout the water column and have values approaching 0.9 in the upper 100 m for SEQ200 and upper 300 m for SEQ400.

Similar observations are made for the deep-water array moorings 1–4 (EAC1–4), that is, the FULL analysis yields a large correlation above 500-m depth. The complex correlation for TRAD is also large at these depths for EAC1–4. Below the 1,000-m depth, the complex correlation coefficients between the observations and the models are small as the model trajectory is barely adjusted toward the observations due to larger observation uncertainty compared to the observed velocity magnitudes and lower model background error uncertainties. The complex correlations of FULL and TRAD in the upper 500 m at EAC5 are slightly smaller compared to other deep mooring sites due to its location outside the main jet and a more variable eddy-dominated circulation.

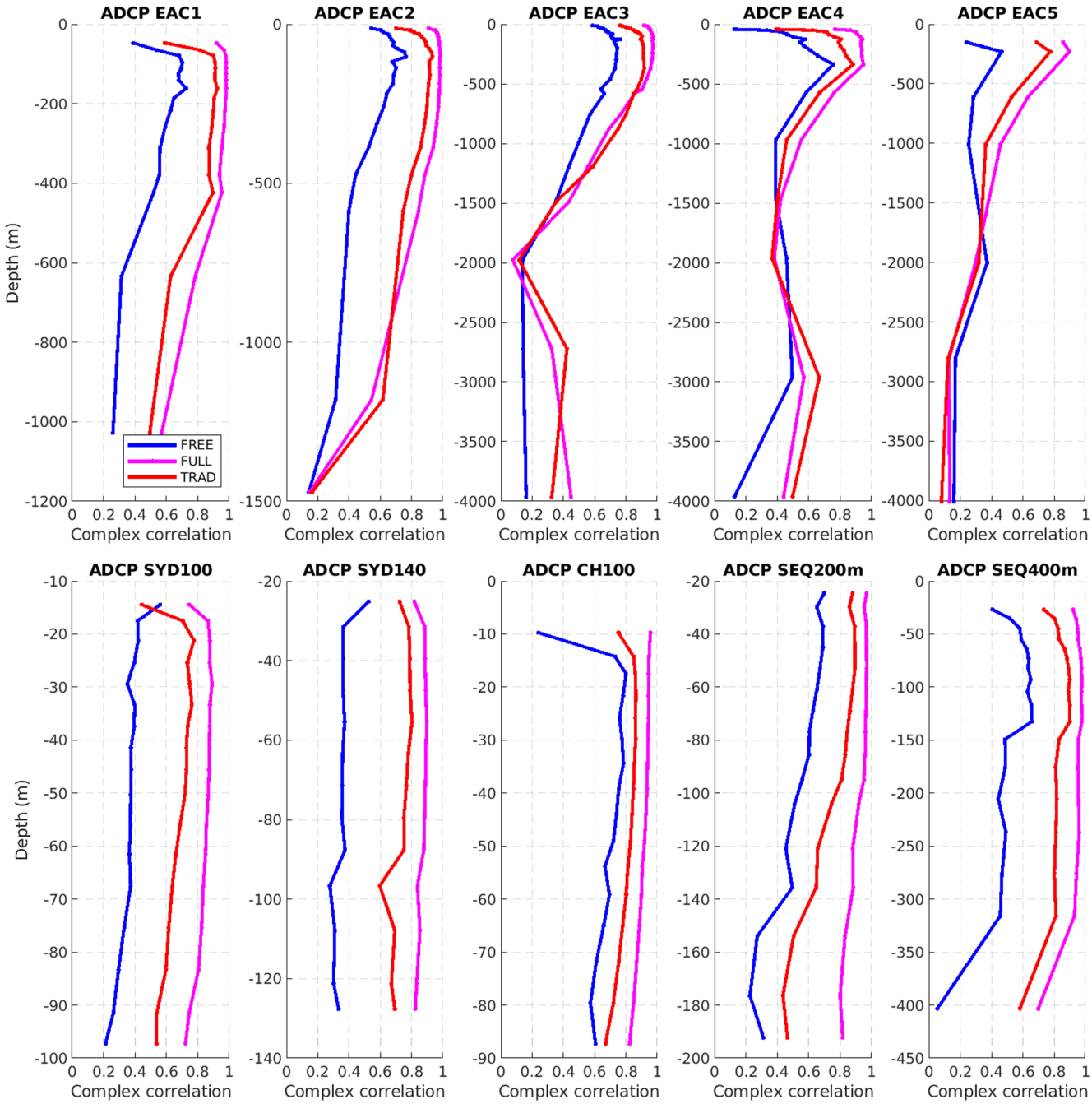

Figure 5. Complex correlations between the observed velocities and the three cases: FREE (blue), TRAD (red), and FULL (magenta) at the mooring locations. TRAD, traditional observations.

The improvement of representing the subsurface velocity of the FULL and TRAD analyses upon the FREE is also shown downstream on the shelf as can be seen for CH100, SYD100, and SYD140 plots. The FULL analysis mean complex correlation across the depths is 0.91 ± 0.04 for CH100 and 0.85 ± 0.03 for Sydney shelf moorings. Overall, the difference in complex correlation of subsurface velocity between FULL and TRAD is quite monotonic with depth, with a difference at about 0.1 for all moorings.

The representation of the subsurface velocity observations was also investigated using variance ellipses shown in Figure 6. Mean velocity vectors, calculated from the time series over 18-month period of

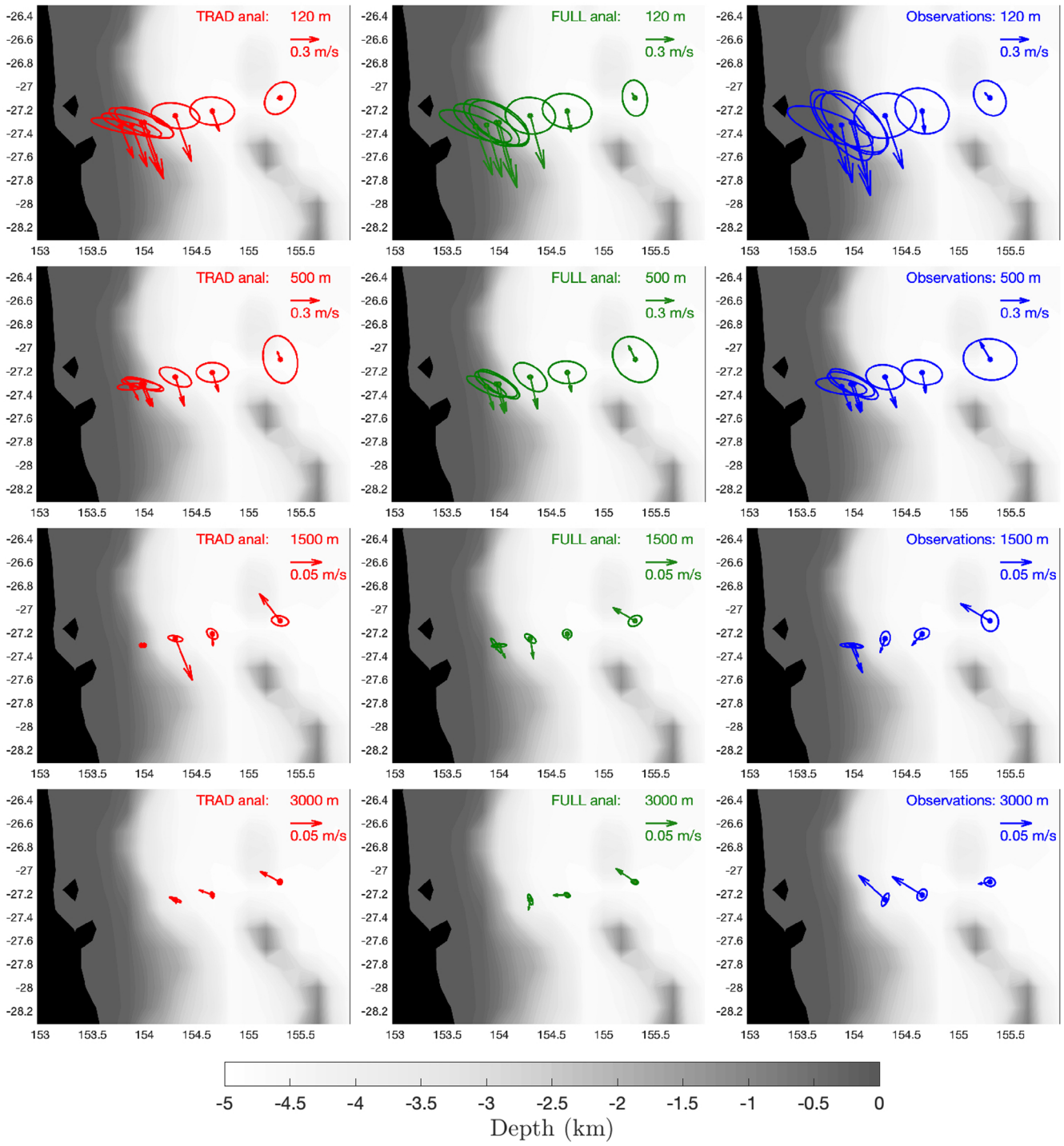

Figure 6. Mean velocity vectors (m/s, arrows) and velocity variance ellipses for 120 m (Row 1), 500 m (Row 2), 1,500 m (Row 3), and 3,000 m (Row 4) for the TRAD (red) and FULL (green) cases, with the observations in blue (by column). TRAD, traditional observations.

mooring deployments, show poleward velocity from the sea surface to 1,500 m across the continental shelf to EAC4 for TRAD, FULL and OBS, and weaker equatorward velocity at EAC5 (155.308E; Figure 6 second row and onward). Both reanalyzes show an agreement with the observed mean velocities down to 1,500 m with the FULL analysis showing better performance in reproducing mean speed and direction. The observations show a stronger poleward velocity at 3,000 m due to a stronger poleward return flow at

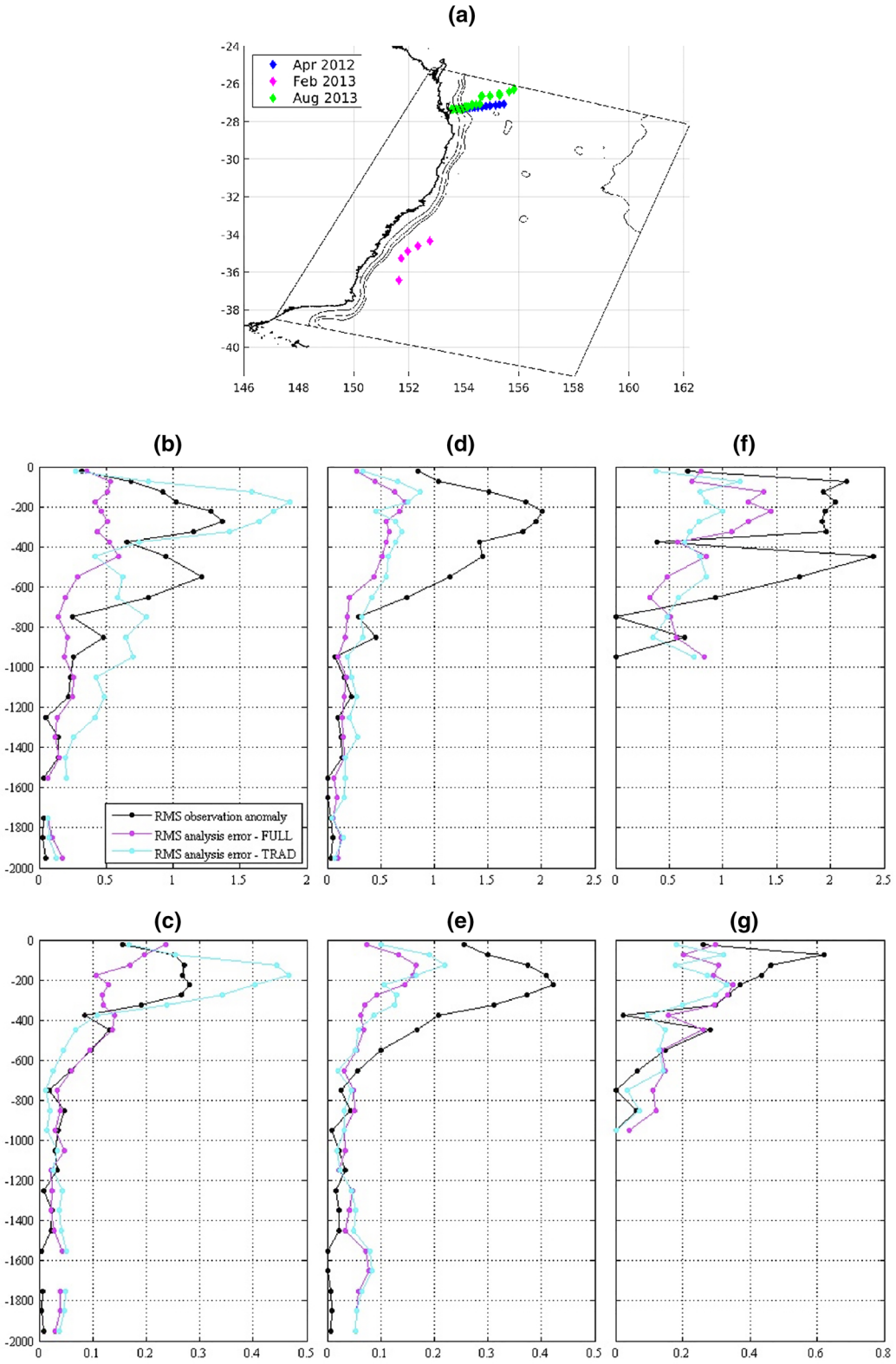

Figure 7. (a) The locations of the CTD casts obtained during three separate time periods as indicated by the colored diamonds. RMS difference between the FULL and TRAD analyses and observations for temperature (middle row) and potential density (bottom row) for April 2012 (b and c), August 2013 (d and e), and February 2013 (f and g). CTD, conductivity–temperature–depth; RMS, root mean square; TRAD, traditional observations.

the base of the EAC core. At these depths, the model velocity values have small variance compared to the defined observation uncertainty, causing the assimilation of the velocity at these depths to provide little constraint to the analysis. Specifically, the nominal minimum observation error for velocity is specified as 0.10 m/s for all depths below 10 m (as described in Kerry et al., 2016), while the specified background error in the deep ocean is of the order of 0.01 m/s. The variance ellipses in the FULL analysis perform well in capturing the observed variability of the EAC in the east-west direction and better match those of the observations.

3.1.3. Nonassimilated Observations

The performance of the FULL and TRAD reanalyzes were further investigated using nonassimilated data obtained from shipboard CTD casts taken on three separate cruises during the assimilation period. The first set of CTD casts comprises of 15 CTDs that were taken as part of the deployment of the EAC array, along the EAC array transect from April 21–27, 2012 (blue diamonds in Figure 7a). The second cruise commenced on February 27–28, 2013 with five CTD casts off the coast of Sydney between 34.3–36.4° S and 151.6–152.8° E (pink diamonds). Finally, we use 28 CTD casts from a cruise between August 21 and 31, 2013, along two transects off Brisbane (green diamonds) at the time the EAC array was removed.

The RMS differences in temperature and potential density between the TRAD and FULL analyses and the nonassimilated CTD observations are reported in the middle and bottom rows of Figure 7, respectively. For the April 2012 period (left column), RMS difference in both temperature and potential density reflects the overall reduction in the model-observations discrepancy in the FULL case relative to the TRAD case. At the depth of 200–400 m, the error for the FULL analysis reduces to about one-third in the magnitude of the RMS error of the TRAD case, which peaks at about 0.45 kg/m^3 at 200-m depth. A similar trend is observed for the RMS temperature error in the April 2012 scenario. This improvement in the FULL case is to be expected as this set of CTD casts were taken at approximately the same coordinates and the same time as the deployment of deep water moorings (EAC1–5). The information gained at the mooring sites propagates to the location of the CTD casts along the EAC array transect via the model adjustment in the data assimilation scheme.

In contrast, the RMS error plots for the second cruise off Sydney 1 year later (Figure 7, right column) shows no significant difference between FULL and TRAD cases. As for the August 2013 cruise, we observe slightly lower error for the FULL case, but the different between the FULL and the TRAD is not as pronounced as in the April 2012 scenario. This is because during August 2013 there is a coherent EAC jet that can be well-constrained by SSH observations in the TRAD case, while the April 2012 scenario is associated with a much weaker circulation regime with weak northward flow across the EAC array.

3.2. Representation of Dynamical Features

In this section, we assess the two reanalyzes in terms of their representation of dynamical features in the EAC in order to determine which features are better captured by the FULL case relative to the TRAD case. We also investigate the contributions of the specific nontraditional observations (glider and HF radar) in constraining the EAC.

3.2.1. Current Transport and Core Structure

The preliminary examination of the EAC core structure and transport for the FULL and the TRAD analyses is done through visualizing the mean of the alongshore velocity as well as the differences of the alongshore velocity mean (FULL−TRAD) at Brisbane (near EAC array), Coffs Harbour, and Sydney cross-shore sections, respectively. Off Brisbane (Figures 8a–8c), the poleward current core in the FULL case is shallower and the jet is narrower near the surface compared to the TRAD case because the FULL is well-constrained by the observations from the EAC array and the shelf moorings. The FULL-TRAD mean velocity difference reveals stronger northward counter-currents, one adjacent to the continental slope and another near the surface offshore of the EAC jet for the FULL case. The alongshore velocity std of both cases (not shown) are comparable with slightly larger velocity variance at the EAC jet and the surface for the FULL case. This information is not carried downstream to Coffs Harbour (Figures 8d–8f), where the core depth in the FULL

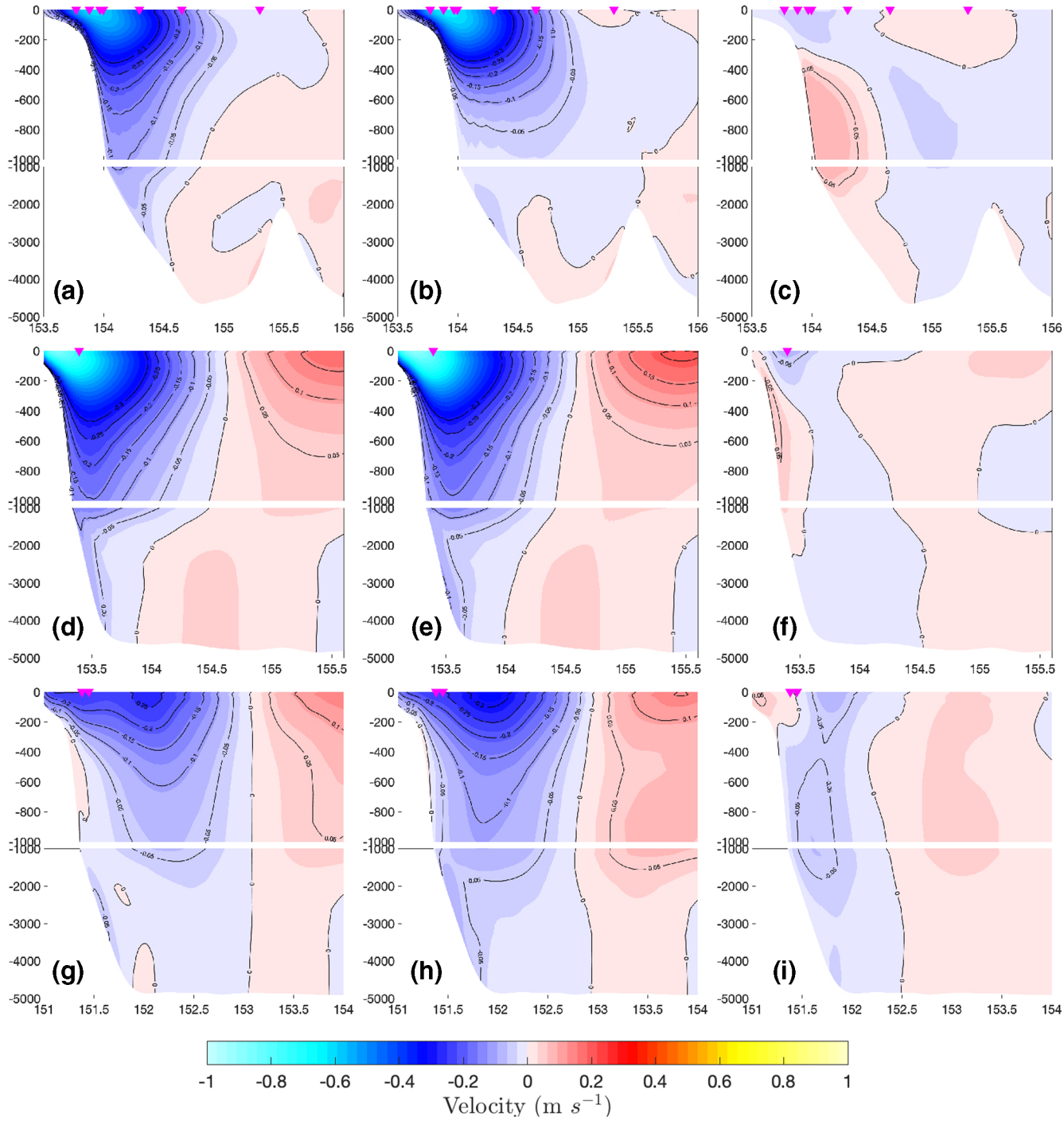

Figure 8. Cross-sections of mean alongshore velocity at (a–c) 27.5°S, the EAC mooring array, (d–f) off 30°S, Coffs Harbour and (g–i) 34°S, Sydney, for the TRAD (a, d, and g) and FULL (b, e, and h) cases, and their difference (c, f, and i). The magenta downward-pointing triangles mark the mooring locations at the surface. EAC, East Australian Current; TRAD, traditional observations.

case is similar to that in the TRAD. The EAC core has deepened compared to off Brisbane and become more unrealistic due to lack of observational constraint. Off Coffs Harbour, the FULL case shows weaker mean poleward transport along the shelf slope to about 2,500-m depth and stronger mean transport in the EAC core. This is related to the HF radar observations off Coffs Harbour that introduce increased cyclonic vorticity inshore of the EAC, as discussed further in Section 3.2.4. Off Coffs Harbour, the FULL case also displays

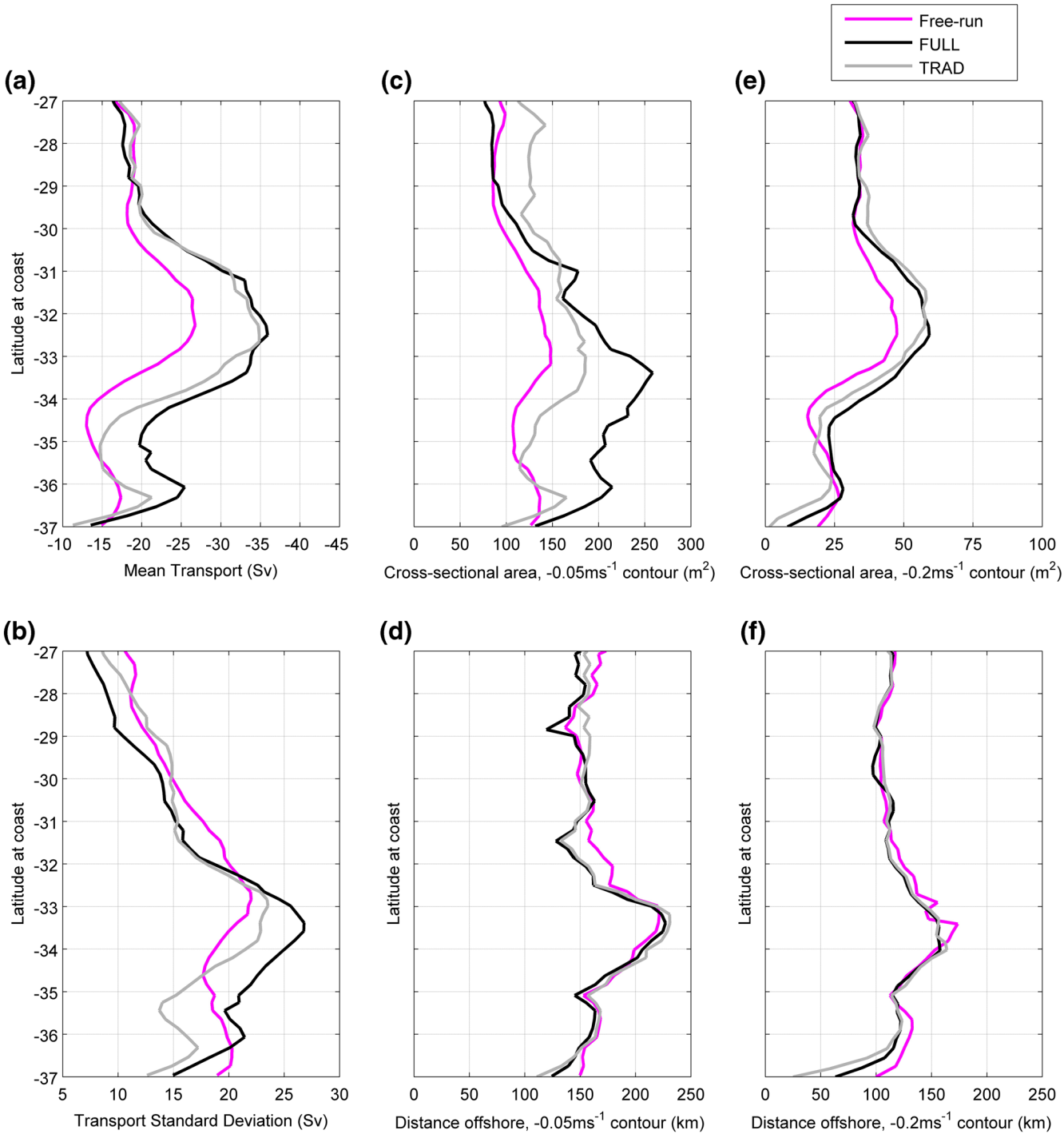

Figure 9. Alongshore transport, EAC core width and cross-sectional area computed every 5 model grid cells (~25 km) from the 22-year free-running ROMS simulation, the FULL analyses and the TRAD analyses. (a) Mean transport (computed inside the −0.05 m/s contour in the alongshore velocity mean), (b) transport standard deviation, (c) the cross-sectional area inside the −0.05 m/s contour in the alongshore velocity mean, (d) the distance offshore of the −0.05 m/s contour in the alongshore velocity mean, (e) the cross-sectional area inside the −0.2 m/s contour in the alongshore velocity mean, (f) the distance offshore of the −0.2 m/s contour in the alongshore velocity mean. The transport is defined as positive (negative) equatorward (poleward). EAC, East Australian Current; ROMS, Regional Ocean Modeling System; TRAD, traditional observations.

larger velocity std near the surface which extends to 155° E (not shown). Off Sydney (Figures 8g–8i), the EAC core is deeper in the FULL case (deeper −0.05 m/s contour). The equatorward flow offshore of the EAC core is stronger in the FULL case across all three sections, the difference increasing poleward.

To quantitatively analyze the EAC core structure, we plot in Figure 9 the time-mean alongshore transport, the mean EAC core width and the cross-sectional area inside the −0.05 m/s contour in the alongshore mean velocity across the latitudes, compared between the FREE22 ROMS simulation, the FULL analyses and the TRAD analyses. The FREE22 simulation (Kerry & Roughan, 2020b) has been shown to provide a realistic representation of the EAC core and its downstream evolution, and therefore, is chosen to be used as the benchmark against the FULL and TRAD reanalyzes in this study. We found that the width of the EAC core is well represented by the assimilation of surface observations (Figures 9d and 9f) but the depth of the core is greater with data assimilation (as reflected in larger transport and cross-sectional area in Figures 9a, 9c, and 9e). In particular, the TRAD analysis overestimates the depth of the EAC core throughout the latitudinal range. In the FULL case, the EAC core depth is constrained by observations at the EAC array but extends deeper than is realistic downstream (even deeper than in the TRAD case). Given that FREE22 provides a realistic representation of the core depth (Kerry & Roughan, 2020a), the unrealistic depth structure in the analyses is likely associated with the cost function being too sensitive to changes in velocity at depth resulting in adjustments to the velocity at depth in the initial conditions.

3.2.2. Cost Function Sensitivities

In the inner loops of the 4D-Var assimilation scheme, the adjoint model computes the sensitivities of the cost function to the increment adjustments (Moore et al., 2011). The conjugate gradient method is used to determine how far to step to evaluate the new increment that reduces the cost function. The new increments are run through the tangent linear model and the cost function is reevaluated. For every assimilation window, the adjoint sensitivity of the cost function to perturbations for each inner loop (1–15) is saved during the assimilation procedure. To interpret these sensitivities, we multiply them by the square root of the average variances for 5-day windows over a long-term (10 years) free running simulation, which provides a realistic perturbation over 5 days (the same model used to compute the prior background error covariances).

We found the temperature sensitivities are surface intensified (not shown) while the sensitivities to alongshore velocity extend to the ocean bottom (Figure 10). This causes the EAC core to extend deeper in the assimilation runs than in the FREE22 case (Figure 9). The EAC core cross-sectional area of the TRAD and the FULL as defined by the area inside −0.2 m/s contour across the latitudes are comparable. However, using the −0.05 m/s contour (Figure 9c), the FULL case exhibits small cross-sectional area north of 30.7°S as the jet is constrained at 27.5°S by the EAC array. Downstream of 30.7°S, the core extends deeper for the FULL case as the high sensitivities to the velocity are observed to extend horizontally in both latitudinal and longitudinal directions (Figures 10e and 10f). The FULL case is constrained around 28°S by observations from the EAC array. However, the area inside the −0.05 m/s contour is greater as the current evolves downstream (Figure 9c) due to these sensitivities (Figures 10e and 10f). The excessive cost function sensitivities to the velocity at depths suggest the need to reduce the velocity background error covariances to improve our estimation of the EAC core structure.

Because the sensitivities are flow dependent, to understand how they are propagated through the ocean we investigate specific assimilation windows. The pattern of high frequency internal waves is revealed by looking at snapshots of the cost function sensitivity as shown in Figure 10g. The assimilation is introducing more HF dynamics as a way of propagating information through the model. Frequency spectra of alongshore velocity at various depths in the middle of the EAC core (not shown) have increased energy at frequencies greater than the inertial frequency. This is characteristic of internal waves, which allow information propagation across the model domain within a 5-day assimilation window (Maiwa et al., 2010; Woodham et al., 2013).

3.2.3. Eddies

To determine how each reanalysis product performs in representing eddies during the assimilation period, and in particular, how the additional data streams (i.e., glider observations) in the FULL case may help improve the eddy representation, a representative sample of eddy events are explored. Three eddy events

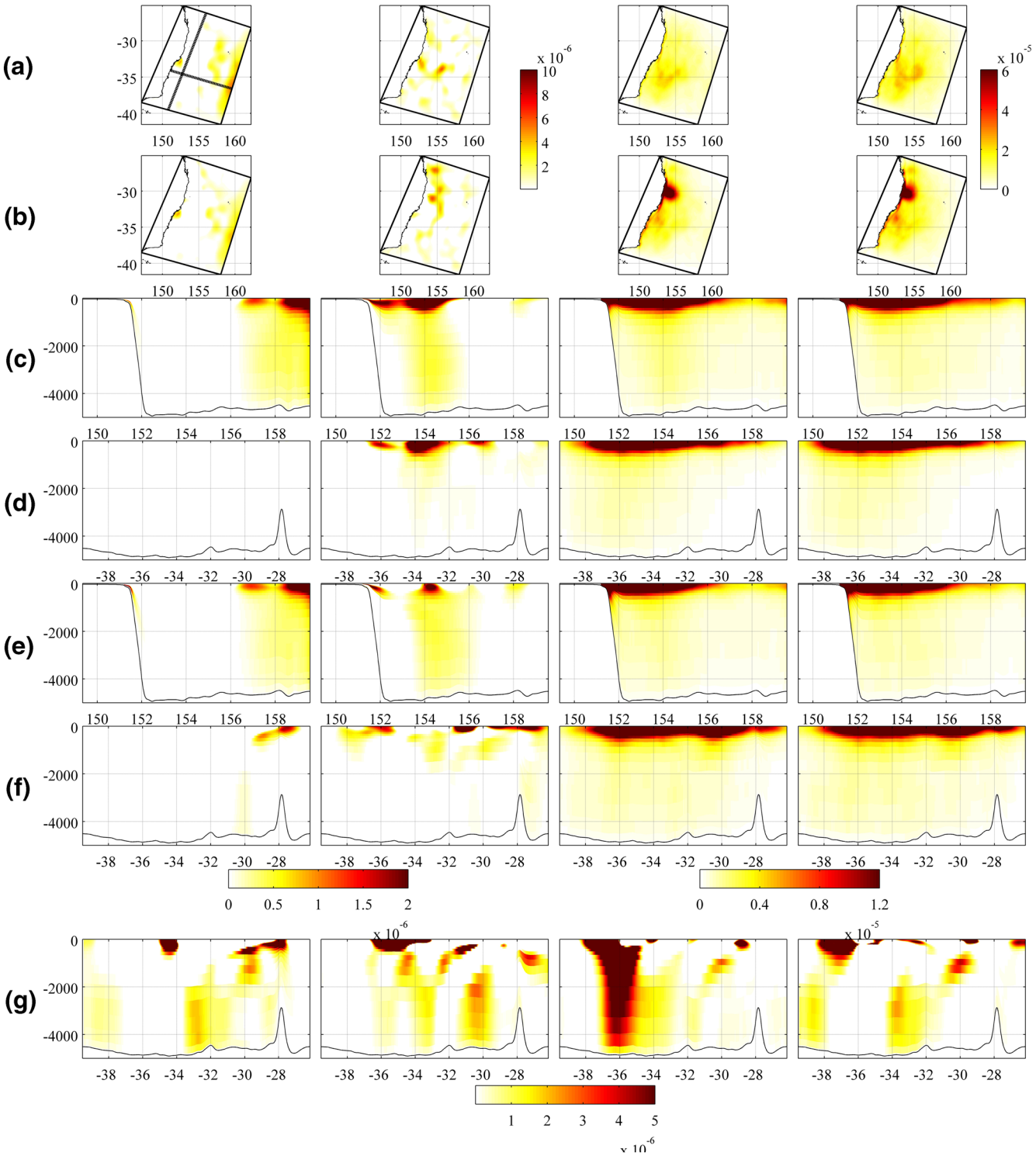

Figure 10. Sensitivities of the cost function multiplied by 5-day standard deviations for alongshore velocity. (a) Sensitivities of TRAD cost function to surface velocity (left to right). Mean sensitivities across all assimilation windows for inner loop 2, mean sensitivities for inner loop 15, standard deviation of sensitivities for inner loop 2, standard deviation of sensitivities for inner loop 15. (b) As in (a) but for FULL cost function. (c) As in (a) but for cross-section through 33.9°S. (d) As in (a) but for alongshore section. (e) As in (c) but for FULL case. (f) As in (d) but for FULL case. (g) Sensitivities of the FULL case cost function for (left to right) assimilation window beginning on the May 24, 2012 inner loop 2, inner loop 15, assimilation window beginning on the April 21, 2012 inner loop 2, inner loop 15. TRAD, traditional observations.

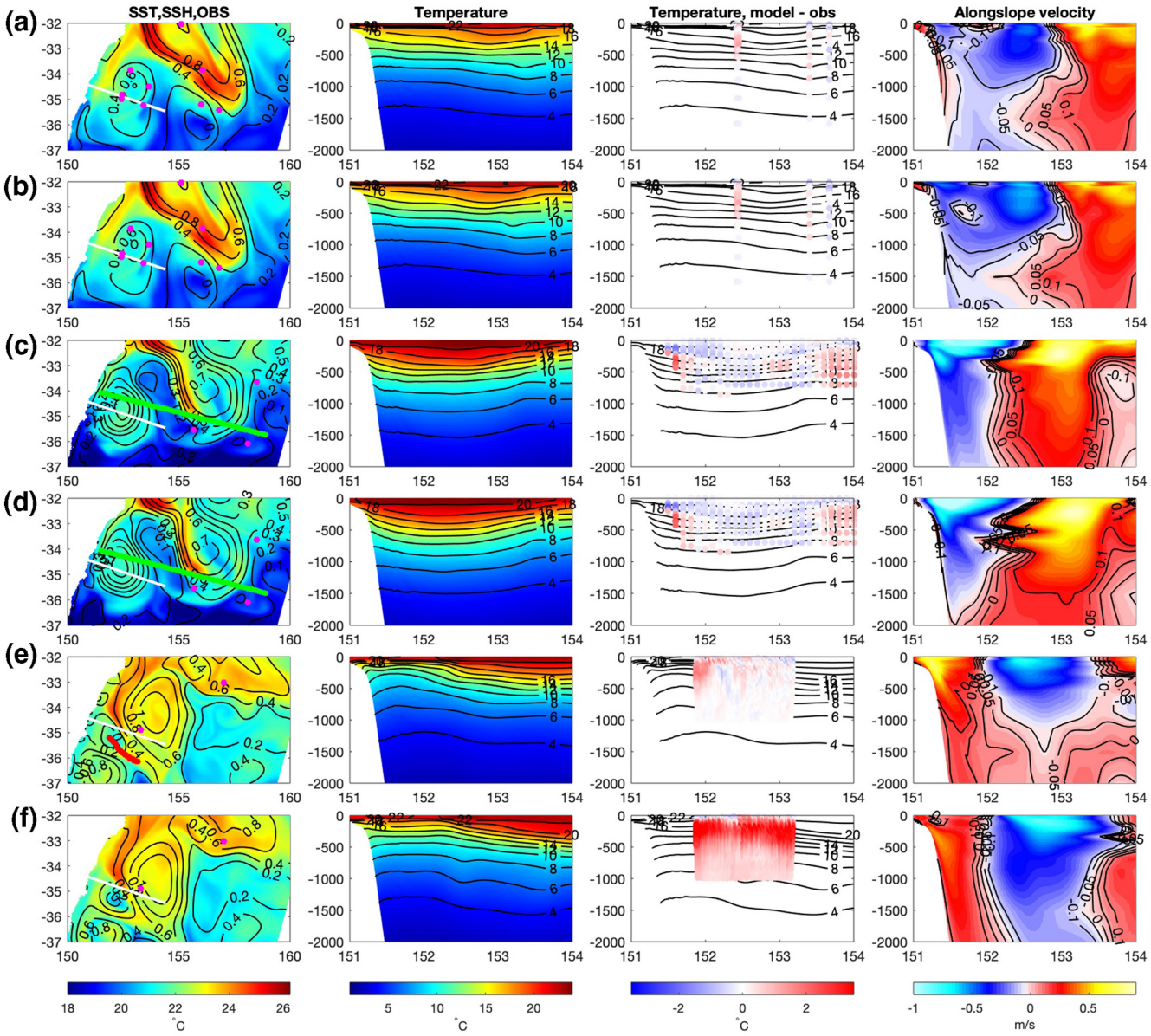

Figure 11. Representations of the eddies at the Sydney section by the models and observations from three different scenarios. Rows a and b: FULL and TRAD analyses, respectively, for January 14, 2012, where only ARGO observations are available. Rows c and d: FULL and TRAD analyses, respectively, for May 25, 2012, where the XBT observations becomes available. Rows e and f: FULL and TRAD analyses, respectively, for April 22, 2013, where the glider observations become available. The first column shows the instantaneous SST (colored), SSH (contoured), and observation locations. The magenta dots are the Argo locations, the green dots are the XBTs, and the red dots (row e) are the gliders. The Sydney cross-section is plotted using thick white lines. TRAD, traditional observations; XBT, expendable bathythermograph.

off the Sydney coast (33.9° S) corresponding to the three available observations scenarios are investigated: (1) January 14, 2012, where four Argos were presented inside the eddy (Figures 11a and 11b), (2) May 25, 2012, where the XBT observations becomes available (Figures 11c and 11d), and (3) April 22, 2013, where the glider observations becomes available for the FULL case and transverse the eddy (Figure 11e).

The results show that for the first two scenarios the eddy representations from both analyses are comparable. This make sense as the Argo and XBT observations are incorporated by both models. The clear difference between the two models appears in the third scenario where the HF glider observations are assimilated in the FULL case. Looking at the structure of the eddy, we see the maximum depth of the −0.05 m/s

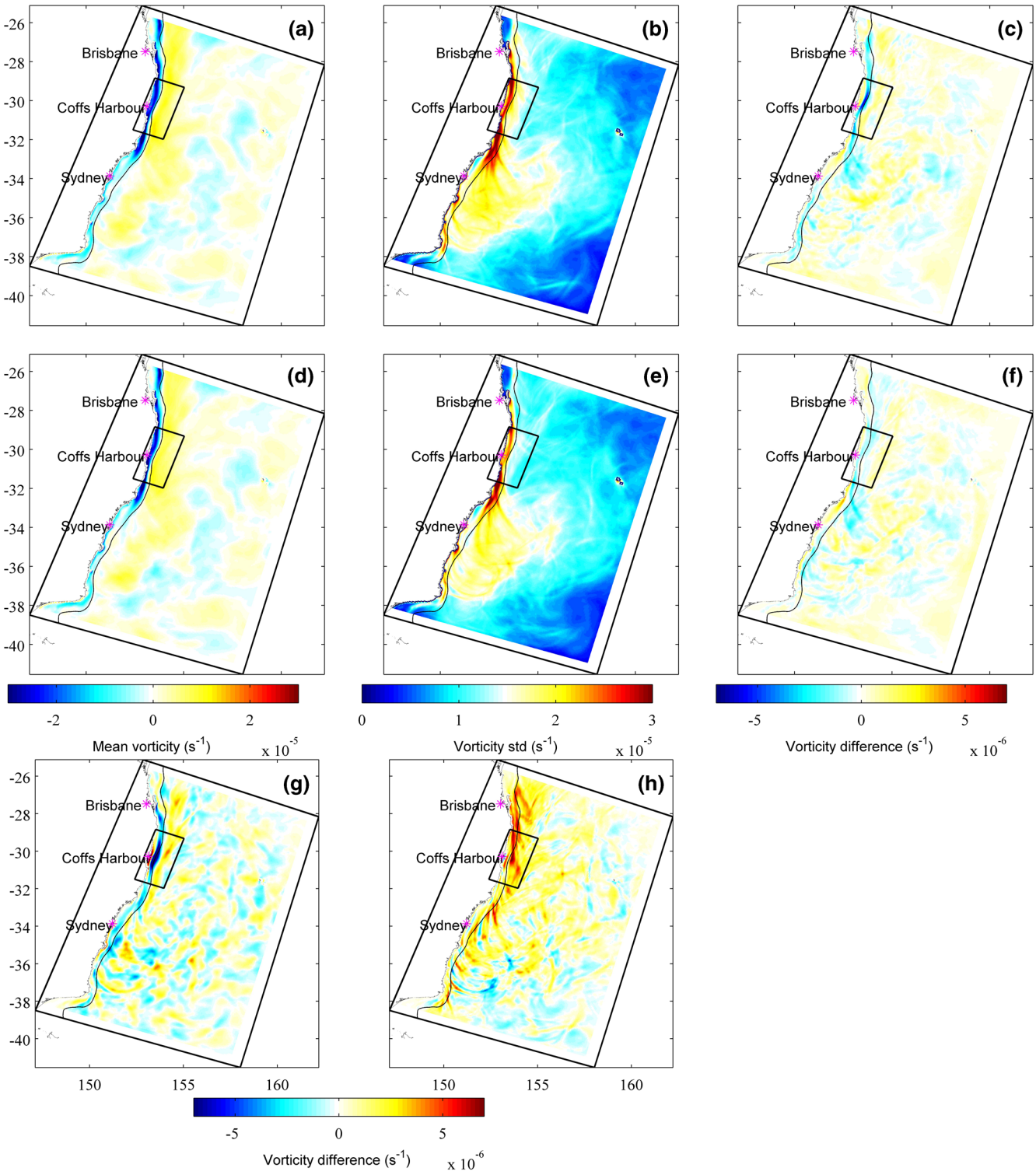

Figure 12. (a) Time-mean surface vorticity from the FULL analyses, (b) standard deviation of surface vorticity computed from 4-h snapshots from the FULL analyses and (c) time-mean surface vorticity difference between the FULL analyses and forecasts. Panels (d–f) are the same as (a–c) but for the TRAD case. (g) Difference in time-mean surface vorticity from the FULL analyses and the TRAD analyses, and (h) difference in the standard deviation of surface vorticity from the FULL analyses and the TRAD analyses. The approximate footprint of the HF radar observations is shown by the black box around Coffs Harbour and the 1,000-m EAC model bathymetry contour is shown. The plots exclude 10 grid cells inside the boundaries (the sponge layer). HF, high frequency; TRAD, traditional observations.

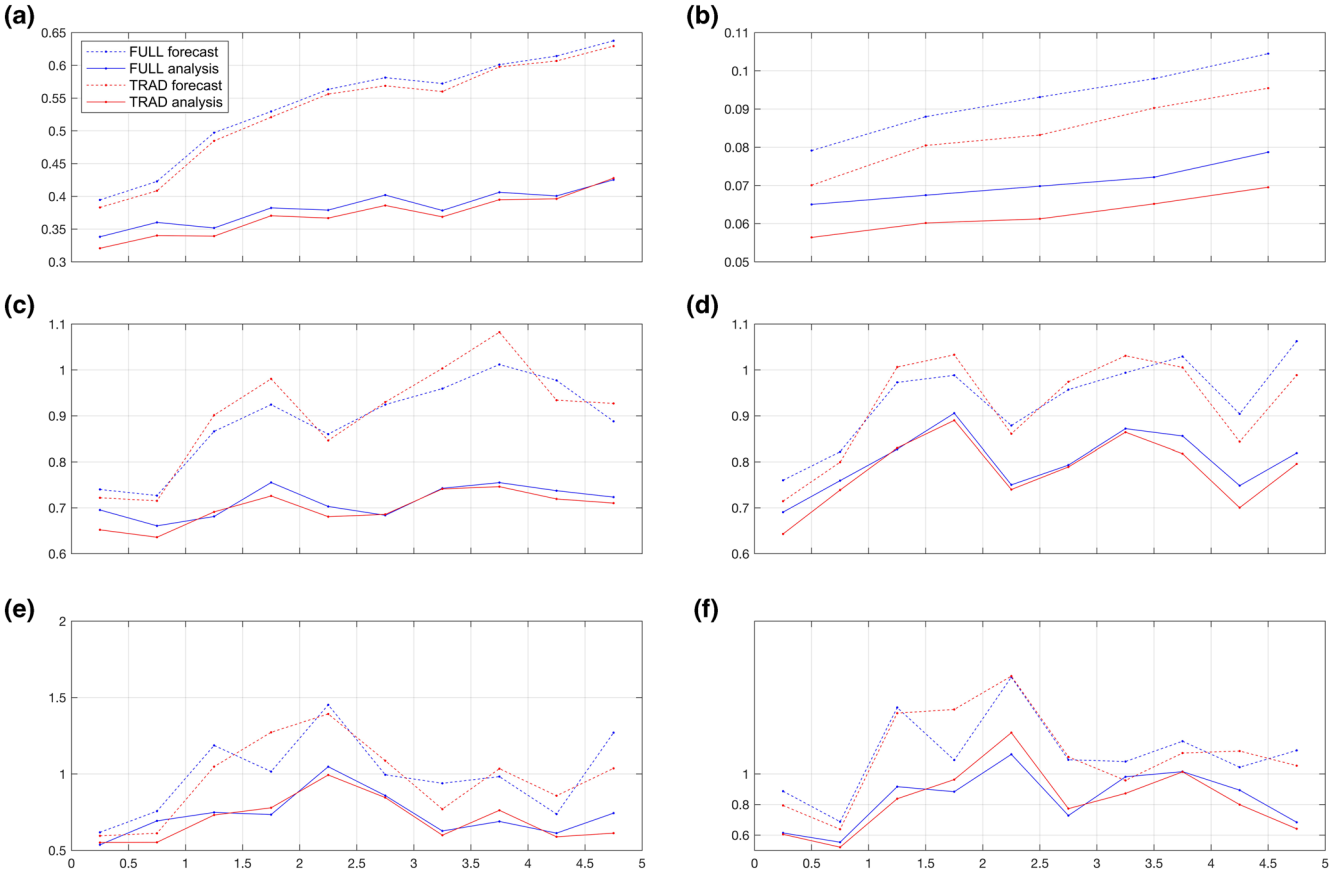

Figure 13. RMS error between the analysis/forecast and the observations, spatially averaged over the model domain, against time from the beginning of the assimilation windows for (a) SST, (b) SSH, (c) Argo in upper 200 m, (d) Argo 200–500 m, (e) XBT in upper 200 m, and (f) XBT 200–500 m. RMS, root mean square; SSH, sea surface height; SST, sea surface temperature; XBT, expendable bathythermograph.

alongshore velocity contour of the FULL case (Figure 11e) is approximately 600 m, which is a realistic eddy depth (Rykova & Oke, 2015), while for the TRAD case the eddy depth descends below 2,000 m. We found that this constraint in the FULL case persists through the 5-day window both in the forecast and the analysis. The information from the gliders not only imposes strong constraints on the depth of the eddy but also strongly alters its meridional extension. The alongshore cross-sections of the eddy (not shown) show that the meridional width of the eddy at the surface, as measured by the distance inside the −0.2 m/s contour, is smaller, from about 3° (333 km) in the TRAD case (no gliders) to roughly 1.3° for the FULL case.

3.2.4. Vorticity

Surface relative vorticity is given by $\zeta = \partial v / \partial x - \partial u / \partial y$, where v and u are the along and cross shore velocity components. Positive vorticity indicates anticyclonic rotation while negative vorticity indicates cyclonic rotation. We compute the surface vorticity from the modeled surface velocity fields every 4 h for the FULL and TRAD cases (Figure 12). In both cases, the analyses show anticyclonic vorticity offshore of the 1,000-m isobath, where the EAC flows poleward and separates from the coast, and cyclonic vorticity over the continental shelf on the inshore edge of the EAC (Figures 12a and 12d). Upstream of the typical EAC separation zone (~32°S), vorticity variability is greatest inshore of the 1,000-m contour (Figures 12b and 12e), where frontal eddies form inshore of the EAC jet (e.g., Roughan et al., 2017). Downstream of the separation region the vorticity variability spreads across the region of elevated eddy activity in the Tasman Sea.

On average over the 2 years, the FULL case has more cyclonic vorticity inshore of the 1,000-m isobath between 28 and 36°S compared to the TRAD case (Figure 12g), indicating an increase in cyclonic rotation inshore of the EAC jet. The sharp vorticity gradient along the inshore edge of EAC derives from the

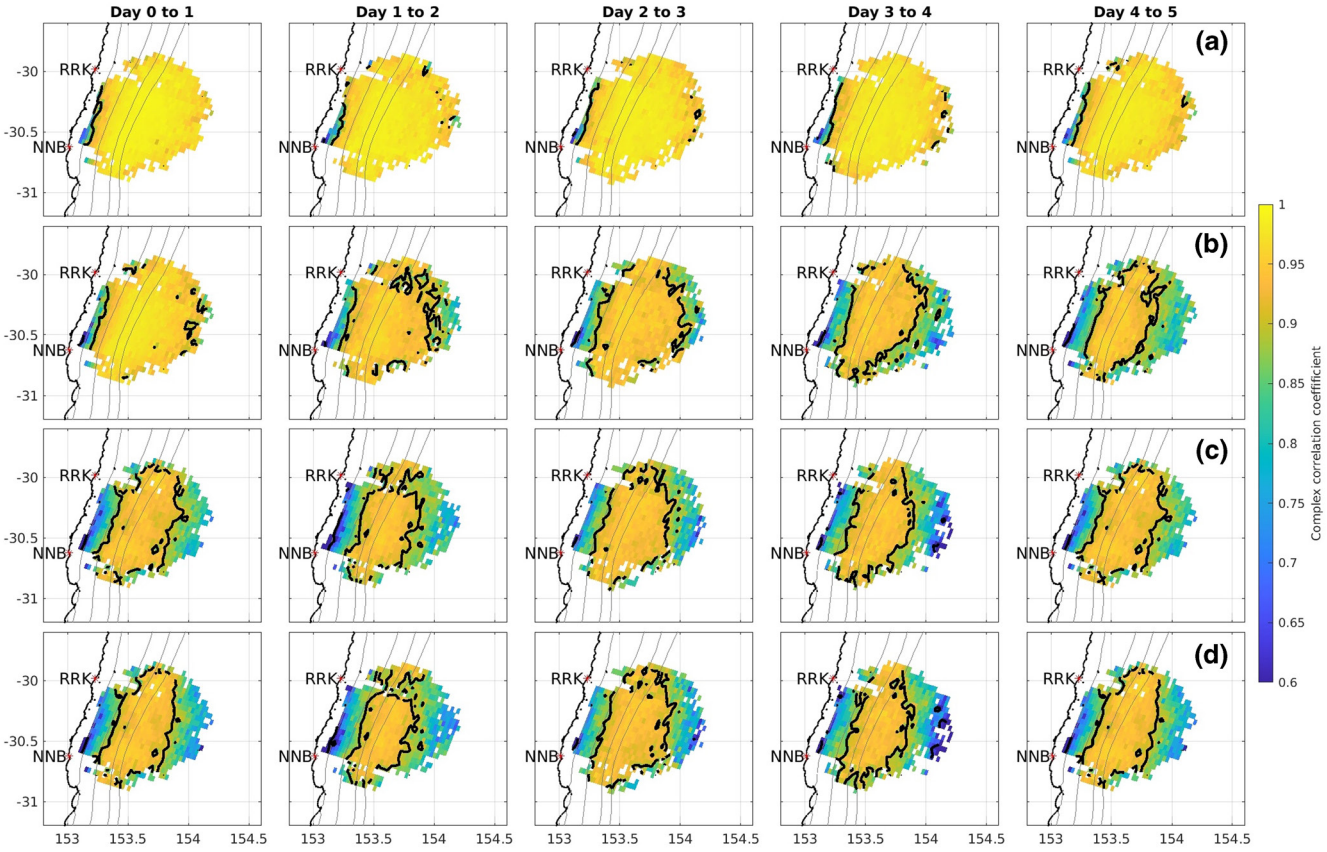

Figure 14. Complex correlation of daily averaged surface velocities measured by the HF radar with FULL reanalysis (row a) and FULL forecast (row b), separated by window day. Complex correlation of daily averaged surface velocities measured by the HF radar with TRAD reanalysis (row c) and TRAD forecast (row d), separated by window day. Black lines show 0.9 complex correlation contour and gray lines show the 70-, 200-, 1,000-, and 2,000-m isobaths. Only grid cells with a minimum of 15 velocity values over the 2-year period are shown, the values inside the 50-m isobath are removed as the computed velocities are unreliable here due to geometric dilution of precision. HF, high frequency; TRAD, traditional observations.

assimilation of HF radar surface radial velocity observations (~29.75–31.25°S) and the information is advected both up and down stream. The FULL case also has greater vorticity variance (Figure 12h) which suggests stronger and more abundant submesoscale features. The advection of relative vorticity is commonly the main contributor to the vorticity balance, as estimated for the Hawaiian Islands by De Souza et al. (2015).

3.3. Predictive Skill

First we assess the predictive skill for the surface variables for the FULL and TRAD cases. Figure 13a shows the RMS error between the SST analyses/forecasts and the observations within a 5 days window, averaged over the 2-year period. The forecasts are initialized by the previous analysis at the end of day 4. The ability to represent the SST observations by the forecasts decays over the 5 days. This may be due to a combination of the circulation features evolving to be in the incorrect locations in the forecast and due to errors in the surface forcing. The TRAD case displays slightly lower RMS SST error both in the forecast and analysis relative to the FULL case. This is caused by the high impact of SST observations on the surface adjustments of the model, especially, in the absence of other nontraditional observations. At the end of the forecast window, the RMS SST error in both cases converges, as the error stems from the forcing and boundary conditions dominating the assimilation system. Similar results can be drawn from Argo and XBT temperature observations (Figures 13c–13f) as these near-surface observations are included in both products. For SSH (Figure 13c), however, better predictive skill of the TRAD case compared to the FULL case is obvious with

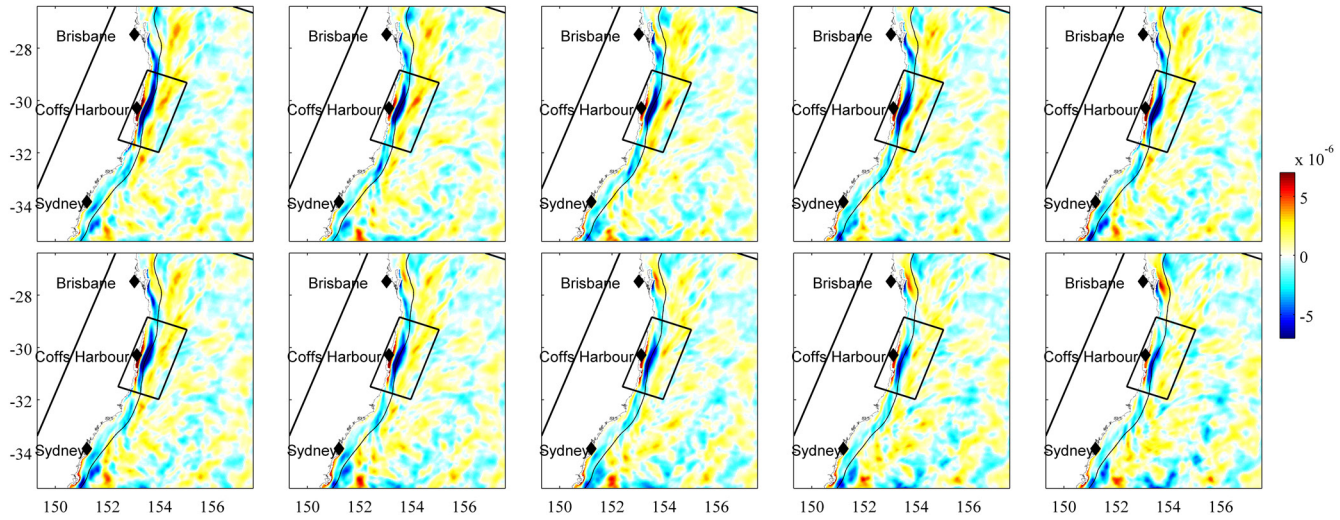

Figure 16. Top row: Difference in time-mean surface vorticity between the FULL and TRAD analyses, separated by window day. Bottom row: Difference in time-mean surface vorticity between the FULL and TRAD forecasts separated by window day. TRAD, traditional observations.

the differences in RMS SSH of about 0.01 m across 5 days. This result is due to a lower volume of SSH data compared to SST.

The predictability of the surface velocity has been assessed and is presented in Figure 14. Panels (a) and (b) show complex correlations of daily averaged surface velocities under the HF radar footprint over a 5 days window for the FULL analysis and forecast, respectively. The FULL analysis demonstrates the ability of the assimilation system to replicate the observations well, with a pointwise complex correlation mostly above 0.9 under the radar footprint. The complex correlation of the FULL forecast, however, starts off with comparable high values as the analysis but gradually degrades over time as observed by a reduction in the area inside the 0.9 complex correlation contour (shown using black lines) in the along shelf direction. The correlations remain high over the EAC core, but decrease elsewhere. Panels (c) and (d) of Figure 14 show the complex correlations of daily averaged surface velocities for the TRAD analysis and forecast, respectively. In the TRAD case, although starting with only a small region of high complex correlation, the correlation does not decay over time for both analysis and forecast. This result is to be expected since there are no HF radar observations to constrain the TRAD reanalysis. It is worth noting that by the fifth day, the FULL forecast complex correlation closely resembles those correlation maps of the TRAD case.

The examination of the predictive capability of the data assimilation models is presented in the terms of the time evolution of complex correlation between the simulated and observed subsurface velocities as shown in Figure 15. The panels (a–d) correspond to SEQ400, EAC2, CH100, and SYD400 moorings, respectively. At SEQ400 where the EAC is typically most coherent, the velocity complex correlation of the FULL forecast (shown in magenta) initially approaches 1 in the upper 300 m similar to its reanalysis counterpart. The correlation decreases with time approaching the smaller complex correlation value of the TRAD case within 5 days. Again, there is no significant change in the complex correlation profile over time in the TRAD case for both the forecasts and the analyses for all mooring sites. The FULL analyses complex correlation is somewhat constant over the 5-day assimilation window for all sites. The complex correlation degrades in the FULL forecast at each mooring, with the faster decay in complex correlation at the CH100 and SYD140 sites which are on the continental shelf downstream of the EAC separation latitude where the circulation is more dynamic and therefore more challenging to predict.

Finally, we also make a comparison of the difference in daily time-mean surface vorticity between the FULL and the TRAD cases with 5-day assimilation window, both in the analysis and the forecast modes (Figure 16). The FULL cases exhibits increased cyclonic vorticity inshore of the EAC in the analyses across the 5 days compared to the TRAD case (Figure 16, top panels) as the TRAD does not assimilate the observations

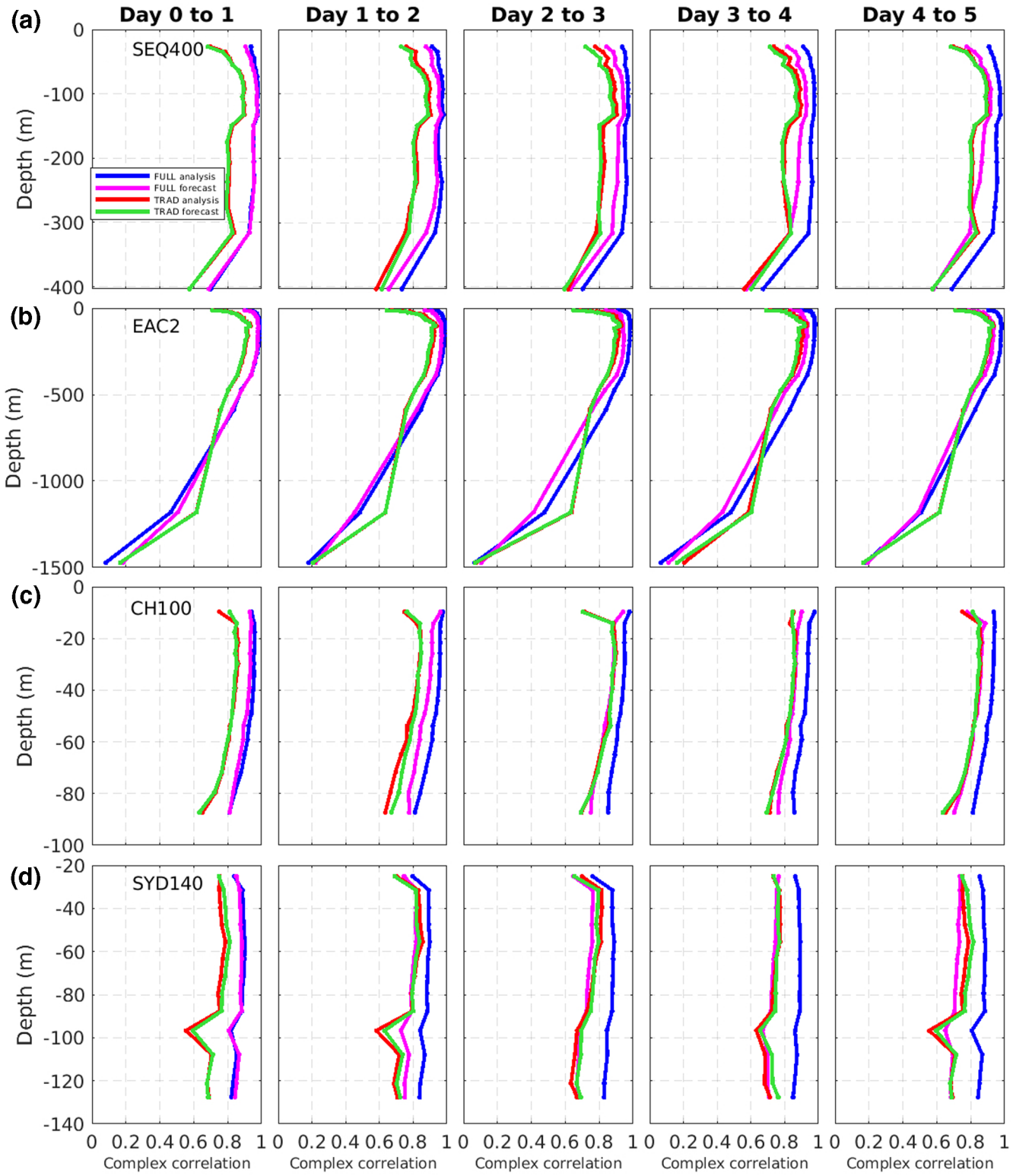

Figure 15. Complex correlations between observed and modeled velocities for the FULL analysis, (blue), FULL forecast (magenta), TRAD analysis (red), and TRAD forecast (green), at the mooring locations, separated by window day (columns). Each row represents a single mooring site. SEQ400 (row a), EAC2 (row b), CH100 (row c), and SYD140 (row d). TRAD, traditional observations.

from the HF radar. In the FULL forecasts, the vorticity gradient inshore of the EAC between 28 and 33°S becomes less sharp over the 5 days although remains sharper than the TRAD forecasts at Day 5.

4. Discussion

4.1. Representation of the Observations by the Reanalysis Products

We showed that the FULL case generally represents observations better than the TRAD case across a number of diagnostics. A notable exception is the surface fields (SSH and SST), which have larger RMS differences in the FULL case than the TRAD case (Figures 2 and 3). This is because the FULL reanalysis also adjusts to the inclusion of the extra (nontraditional observations) that add additional features to the reanalysis and thus affect the longer scales resolved by the observed SSH and SST. As the number of satellite-derived SST observations is far greater than any other dataset, SST dominates the cost function compared to SSH, so the difference between the representation of SST in the TRAD and the FULL cases is less than the difference for SSH. This can be addressed by subsampling the satellite SST observations to reduce the volume of dependent observations and reduce their dominance compared to SSH.

Over the EAC core region and in the upper 1,000 m the TRAD analysis performs considerably better than the FREE case (Figure 5), indicating that assimilation of surface observations (specifically SSH) provides improved representation of velocity on the shelf and in the upper water column influenced by the mesoscale circulation. This is consistent with the results of Moore et al. (2011), who showed that SSH observations have the largest impact on the accurate representation of shelf transport, and Oke and Schiller (2007), who established that altimetry observations are essential for resolving mesoscale circulation. Furthermore, comparison of the TRAD analysis with the nonassimilated CTD observations (August 2013 scenario) further highlights the importance of the satellite SSH observations by showing that the errors between the TRAD analysis and the observations only differs slightly to the FULL case (Figure 7, middle). We believe that this is due to the strong geostropic flow being well constrained by the SSH observations, in comparison to the period of weak flow (April 2013) which is poorly represented by the TRAD case.

The inclusion of subsurface moored observations in the FULL case has a strong influence on the adjustment of the EAC flow. As such, the FULL analysis has a better representation of the mean jet at the mooring locations (Figures 5 and 6). However, at abyssal depths (below 3,000 m) the FULL case underestimates the return flow in the observations due to large observation uncertainty in comparison with the background error covariance. This shows that representing currents at abyssal depths remains a challenge.

4.2. EAC Core Structure and Cost Sensitivity

The adjustment in the state vector by 4D-Var alters the model trajectory as a result of the system attempting to better represent the observations while abiding by the model physics. The flow-dependent nature of 4D-Var means that information can propagate away from observation sites by various oceanic processes, which include, but are not limited to, advection, barotropic and baroclinic waves (Kerry et al., 2018; Kurapov et al., 2011). Consequently, significant changes in the dynamic features of the EAC both downstream and upstream of the added observations can easily be envisaged.

While both FULL and TRAD analyses match the FREE22 well in terms of distance offshore of the EAC core (Figures 9d and 9f), both cases overestimate the transport and EAC cross-sectional area (inside the −0.05 m/s contour) at most latitudes (Figures 9a, 9c, and 9e). The increased cross-sectional area estimates result in increased transport which further indicates that 4D-Var overadjusts the velocities at depths. The adjoint sensitivities of the cost function to alongshore velocity are shown to extend from the surface to the ocean bed (Figure 10), causing the EAC core to extend deeper in the assimilations than in the more realistic freely evolving simulation, leading to increased transport. The EAC core has also been found to extend over the full depth of the ocean (4,500 m) in the BRAN reanalysis product which makes use of an Ensemble Optimal Interpolation assimilation scheme (Oke et al., 2008; Oke & Griffin, 2011). To prevent this issue, it is desirable to reduce the velocity background error covariances in future assimilation setups. Despite our considerable effort to prescribe reasonable error covariance models, these drawbacks remind us of the importance of constantly updating the error covariances as new information becomes available. Determining the error

covariances for optimal estimations is indeed an on-going and one of the most challenging research areas in data assimilation (Bousserez et al., 2015; Dreano et al., 2017; Moore et al., 2012; Ngodock et al., 2020).

4.3. Eddies and Submesoscale Variability

Traditionally the depth extent of eddies in the EAC has been limited to the "level of no motion," which has long been believed to be approximately 2,000-m deep (Bowen et al., 2005; Ridgway & Dunn, 2003). The observation-based study of Rykova and Oke (2015) showed that in the EAC region the temperature anomalies within anticyclonic and cyclonic eddies can reach up to 1,500 and 2,000 m, respectively. However, in numerical models such as BRAN, the depth extent of these eddies tends to be over represented as discussed by Roughan et al. (2017), sometimes extending the full depth of the water column (4,000 m) as shown in Oke and Griffin (2011).

In our case, the added sensitivity of the assimilation system at depth negatively affects the estimation of the eddy depth and structure. Both TRAD and FULL cases shown unrealistic eddy depth (exceeding 2,000 m) through the imperfect design of the error covariance matrices. The deep glider data (FULL) was found to be effective in constraining the eddy structure, including depth estimates. The FULL analysis estimates the EAC core depth (as measured by the −0.05 m/s contour) at the location of the studied eddy to be around 600 m. The diameter of this depth constraint in the alongshore direction is about 100 km, corresponding to the spatial length scale of the studied eddy (111 km) and in agreement with the typical length scale of energetic mesoscale eddies (100–200 km) in WBCs globally (Chelton et al., 2011a, 2011b; Roughan et al., 2017).

The strong constraint of the transport by ocean gliders found in this study is consistent with the results reported in Powell (2017), where, despite the small percentage of data, the inclusion of subsurface sea glider observations accounted for 23% of the total impact on transport adjustment. The glider data are also known to be very effective in constraining isopycnal tilt across the transport section. In this study, the benefit of including glider data is shown the representation of eddy depth. It is also noteworthy that the glider observations should be used with caution. The work by Pasmans et al. (2019), in which the reanalysis using the combination of surface and glider observations was skillful in estimating and forecasting the subsurface ocean features, has demonstrated that assimilating glider observations without the surface observations can create erroneous eddy variability that will deteriorate forecast performance.

Kerry et al. (2020b) shows that the sharper across-current vorticity gradient within the EAC leads in turn to more intense submesoscale features growing on its inshore side. The submesoscale variability growing from jet instabilities manifested over the continental shelf are not resolved by the model grid but are captured by the observations. As such, data assimilative models can recover these submesoscale structures in the analysis mode. We show this in the FULL case where assimilation of HF radar velocities improves the vorticity gradients. The FULL reanalysis also has greater vorticity variance which suggests stronger and more abundant submesoscale flows originating from sharper cross-current vorticity gradient. However, the FULL forecast was unable to reproduce the sharp cyclonic band inshore of the EAC after 5 days. This suggests the model resolution of 2.5–6 km is too coarse to maintain the vorticity gradient observed by the HF radar.

4.4. Predictive Skill

Our results show that the predictive skill is similar for SST, SSH, and subsurface temperature (Figure 13) for both the TRAD and the FULL cases, and both exhibit similar diverging trends between the forecast and the analysis. A slightly smaller 5-day RMS error for the TRAD case is expected as the FULL also fits the high volume nontraditional observations.

Under the radar footprint, the predictive performance of the surface velocity in the FULL forecast decays to the same accuracy level of the TRAD forecast within 5 days (Figure 14). This suggests that introducing high-resolution HF radar observations does not contribute to the predictive skill beyond the spatial and temporal resolution of the EAC model as the error from the boundaries and forcing quickly dominate the forecast. The complex correlation of the subsurface velocity at several mooring sites, separated by day from the beginning of the forecast window (Figure 15) shows that the FULL forecast also decays to the same accuracy as the TRAD within 5 days. However, notable are the different decay rates at different sites in the

FULL analysis, where the flow over the shelf (at the mooring locations) shows much faster degradation (in complex correlation) compared to that of flow in deep water (at the deepwater mooring locations). This is due to the more complex and fine-scale dynamics over the shelf which are more difficult to predict and not adequately resolved by the EAC model.

Surface vorticity is another useful metric, which in the FULL case, shows the adjustments to the velocity initial conditions and wind stress forcing allow the analysis to better represent the cyclonic band inshore of the EAC and achieve greater cyclonic vorticity over the shelf slope (Figure 12b). However, the wind forcing adjustments made by the model are not considered to be realistic dynamical drivers for maintaining sharp cyclonic fronts inshore of the EAC. It is likely that increased model resolution is required to better represent these small-scale fast-evolving dynamics (as also suggested by Sandery and Sakov [2017] and Kerry et al. [2020b]).

5. Summary and Conclusions

The goal of an advanced data assimilation technique such as 4D-Var is to provide an estimate of the ocean state that represents the observations in the correct dynamical context. Considerable advances in data assimilation techniques, increased computing power to allow higher resolution models, and the availability of new observation platforms has motivated the inclusion of such observations in model estimates and predictions. The challenge is to configure the ocean model and its data assimilation system such that the observations can be represented in the correct dynamical context and that these dynamics can be resolved in forecast mode. This study builds on the work of Kerry et al. (2016, 2018) and takes a simpler yet more practical approach to observation impact by comparing the state-estimates and forecasts of the system that assimilates all available observations (the FULL case) and a system that assimilates only the traditionally available observations (the TRAD case).

While the FULL system provides the best representation of the observations that it assimilates (from HF radar, the EAC deepwater array, shelf moorings, and gliders), we show that the TRAD system also provides improved representation of velocity on the shelf and in the upper 1,000 m for the deepwater moorings and improved estimates of surface velocities over the EAC core region observed by the HF radar array, when compared to the free-running model. The relative performance of the FULL and TRAD systems compared to subsurface CTD cast observations, not assimilated in either system, is dependent on the circulation regime. The TRAD case performs equally as well as the FULL when a strong coherent EAC jet can be well constrained by SSH observations, but during periods of weak flow the subsurface structure is not well represented by TRAD case compared to the FULL. The width of the EAC core is well represented by the assimilation of surface observations in both the TRAD and the FULL systems. While the free running model provides a better representation of the EAC core depth (Kerry & Roughan, 2020a), both reanalysis products overestimate the core depth of the EAC and its eddies due to excessive cost function sensitivity to velocity at depth. In the FULL case, the EAC core depth is well constrained by observations from the EAC array but performs less well downstream where the EAC core and eddies extend deeper than is realistic, while in the TRAD case the EAC core is too deep throughout its latitudinal extent. Eddy depth is well represented in eddies sampled by the glider observations in the FULL case.

In forecast mode, corrections made to the subsurface ocean structure by the assimilation of data from moorings or gliders relax on time scales of 5 days to the same as TRAD. Assimilation of surface radial velocities in the FULL case produces a sharper vorticity gradient inshore of the EAC at the HF radar location and upstream and downstream, but this improvement does not persist throughout the 5 days forecast window as the free running model is unable to resolve the sharp vorticity gradients observed by the HF radar. After 5 days, the skill in surface velocity predictions under the HF radar footprint is the same for the FULL and TRAD cases.

While the goal of 4D-Var is to fit to the observations while correctly representing the circulation dynamics, the results of this study highlight the challenges associated with assimilating observations that can introduce unrealistic dynamics into the model to achieve a fit to the observations. Improvements to the assimilation configuration are required to overcome this. In particular, this study suggests we should reduce the

velocity background errors at depth to achieve better representation of the depth of the EAC core and its eddies, which are well represented in the free running model.

Furthermore, these results highlight the challenges associated with the assimilation of a range of datasets. For example, with the HF radar data assimilation, although the data were thinned to have the same spatial resolution as the model, the model is unable to reproduce the sharp vorticity gradient observed. A higher resolution numerical model is likely required to reap the benefits of assimilation of surface radial velocities in forecast mode. Indeed, while predictions of mesoscale eddies, which are typically slowly evolving, are mostly dependent on correct representation of their initial state, predicting more rapidly evolving features requires focus on reducing model error.

Overall, while the FULL case provides a superior reanalysis due to the inclusion of a number of data from newly available nontraditional observation platforms, the TRAD system performed equally well for forecasts with lead times of 5 days. Further work is required on the FULL assimilation system to better represent the circulation dynamics such that superior forecasts can be achieved.

Data Availability Statement

Observations are available at www.aodn.org.au. Argo data were collected and made freely available by the International Argo Program and the national programs that contribute to it. (http://www.argo.ucsd.edu, http://argo.jcommops.org). The Argo Program is part of the Global Ocean Observing System (http://doi.org/10.17882/42182). Model output is made available for research purposes and is accessible at https://doi.org/10.26190/5e683944e1369 and https://doi.org/10.26190/5ebe1f389dd87. Use of the FREE22 model output should be cited as Kerry and Roughan (2020b). Use of the FULL reanalysis output should be cited as Kerry et al. (2020a).

Acknowledgments
This research and Adil Siripatana were partially supported by the Australian Research Council Industry Linkage grant #LP170100498 to Moninya Roughan, Colette Kerry, and Shane Keating. Prior model development was supported by the Australian Research Council grants #DP140102337 and #LP160100162. CSIRO Marine and Atmospheric Research and Wealth from Oceans Flagship Program, Hobart, Tasmania, Australia provided BRAN3p5 output for boundary conditions. The observations were sourced from the Integrated Marine Observing System (IMOS) – IMOS is enabled by the National Collaborative Research Infrastructure (NCRIS), supported by the Australian Government. It is operated by a consortium of institutions as an unincorporated joint venture, with the University of Tasmania as Lead Agent. www.imos.org.au. We acknowledge AVISO for the Delayed-time SLA data. The Ssalto/Duacs altimeter products were produced and distributed by the Copernicus Marine and Environment Monitoring Service (CMEMS) (http://www.marine.copernicus.eu).

References

Bousserez, N., Henze, D. K., Perkins, A., Bowman, K. W., Lee, M., Liu, J., et al. (2015). Improved analysis-error covariance matrix for high-dimensional variational inversions: Application to source estimation using a 3D atmospheric transport model. *Quarterly Journal of the Royal Meteorological Society*, *141*(690), 1906–1921. https://doi.org/10.1002/qj.2495

Bowen Melissa M., Wilkin John L., Emery William J. (2005). Variability and forcing of the East Australian Current. *Journal of Geophysical Research: Oceans*, *110*(C3). http://dx.doi.org/10.1029/2004jc002533

Cetina-Heredia, P., Roughan, M., van Sebille, E., & Coleman, M. A. (2014). Long-term trends in the East Australian Current separation latitude and eddy driven transport. *Journal of Geophysical Research: Oceans*, *119*(7), 4351–4366. http://dx.doi.org/10.1002/2014jc010071

Chelton, D. B., Gaube, P., Schlax, M. G., Early, J. J., & Samelson, R. M. (2011a). The influence of nonlinear mesoscale eddies on near-surface oceanic chlorophyll. *Science*, *334*(6054), 328–332. https://doi.org/10.1126/science.1208897

Chelton, D. B., Schlax, M. G., & Samelson, R. M. (2011b). Global observations of nonlinear mesoscale eddies. *Progress in Oceanography*, *91*(2), 167–216. https://doi.org/10.1016/j.pocean.2011.01.002

De Souza, J. M. A. C., Powell, B., Castillo-Trujillo, A. C., & Flament, P. (2015). The vorticity balance of the ocean surface in Hawaii from a regional reanalysis. *Journal of Physical Oceanography*, *45*, 424–440.

Di Lorenzo, E., Moore, A. M., Arango, H. G., Cornuelle, B. D., Miller, A. J., Powell, B., et al. (2007). Weak and strong constraint data assimilation in the inverse Regional Ocean Modeling System (ROMS): Development and application for a baroclinic coastal upwelling system. *Ocean Modelling*, *16*(3), 160–187. https://doi.org/10.1016/j.ocemod.2006.08.002

Dreano, D., Tandeo, P., Pulido, M., Ait-El-Fquih, B., Chonavel, T., & Hoteit, I. (2017). Estimating model-error covariances in nonlinear state-space models using Kalman smoothing and the expectation-maximization algorithm. *Quarterly Journal of the Royal Meteorological Society*, *143*(705), 1877–1885. https://doi.org/10.1002/qj.3048

Feron, R. C. V. (1995). The Southern Ocean western boundary currents: Comparison of fine resolution Antarctic model results with Geosat altimeter data. *Journal of Geophysical Research*, *100*(C3), 4959–4975.

Haidvogel, D. B., Arango, H. G., Hedstrom, K., Beckmann, A., Malanotte-Rizzoli, P., & Shchepetkin, A. F. (2000). Model evaluation experiments in the north Atlantic basin: Simulations in nonlinear terrain-following coordinates. *Dynamics of Atmospheres and Oceans*, *32*, 239–281.

Haney, R. L. (1991). On the pressure gradient force over steep topography in sigma coordinate ocean models. *Journal of Physical Oceanography*, *21*, 610–619.

Imawaki, S., Bower, A. S., Beal, L., & Qiu, B. (2013). Chapter 13 - western boundary currents. In G. Siedler, S. M. Griffies, J. Gould, & J. A. Church (Eds.), *Ocean circulation and climate, International Geophysics* (Vol. 103, pp. 305–338). Academic Press. https://doi.org/10.1016/B978-0-12-391851-2.00013-1

Kerry, C. G., Powell, B. S., Roughan, M., & Oke, P. R. (2016). Development and evaluation of a high-resolution reanalysis of the East Australian Current region using the Regional Ocean Modeling System (ROMS 3.4) and incremental strong-constraint 4-dimensional variational (IS4D-var) data assimilation. *Geoscientific Model Development*, *9*, 3779–3801.

Kerry, C., & Roughan, M. (2020a). Downstream evolution of the East Australian Current system: Mean flow, seasonal, and intra-annual variability. *Journal of Geophysical Research: Oceans*, *125*(5), e2019JC015227. https://doi.org/10.1029/2019JC015227

Kerry, C., & Roughan, M. (2020b). *A high-resolution, 22-year, free-running, hydrodynamic simulation of the East Australia Current system using the Regional Ocean Modeling System*. UNSW Dataset 2020. https://doi.org/10.26190/5e683944e1369. Retrieved from https://researchdata.ands.org.au/high-resolution-22-ocean-modelling

Kerry, C., Roughan, M., & Powell, B. S. (2018). Observation Impact in a Regional Reanalysis of the East Australian Current System. *Journal of Geophysical Research: Oceans*, *123*(10), 7511–7528. http://dx.doi.org/10.1029/2017jc013685

Kerry, C., Roughan, M., & Powell, B. (2020b). Predicting the submesoscale circulation inshore of the East Australian Current. *Journal of Marine Systems*, *103*, 286. https://doi.org/10.1016/j.jmarsys.2019.103286

Kerry, C., Roughan, M., Powell, B., & Oke, P. (2020a). *A high-resolution reanalysis of the East Australian Current system assimilating an unprecedented observational data set using 4D-var data assimilation over a two-year period (2012-2013)*. UNSW Dataset 2020. https://doi.org/10.26190/5ebe1f389dd87. Retrieved from https://researchdata.ands.org.au/high-resolution-reanalysis-version-2017

Kistler, R., Kalnay, E., Collins, W., Saha, S., White, G., Woolen, J., et al. (2001). The NCEP/NCAR 50-year reanalysis. *Bulletin of the American Meteorological Society*, *82*, 247–268.

Kurapov A. L., Foley D., Strub P. T., Egbert G. D., & Allen J. S. (2011). Variational assimilation of satellite observations in a coastal ocean model off Oregon. *Journal of Geophysical Research*, *116*(C5). http://dx.doi.org/10.1029/2010jc006909

Le Dimet, F., & Talagrand, O. (1986). Variational algorithms for analysis and assimilation of meteorological observations: Theoretical aspects. *Tellus*, *38A*, 97–110.

Lee, T. N., Atkinson, L. P., & Legeckis, R. (1981). Observations of a gulf stream frontal eddy on the Georgia continental shelf, April 1977. *Deep Sea Research Part A. Oceanographic Research Papers*, *28*(4), 347–378. https://doi.org/10.1016/0198-0149(81)90004-2

Lewis, J. M., & Derber, J. C. (1985). The use of adjoint equations to solve a variational adjustment problem with advective constraints. *Tellus A: Dynamic Meteorology and Oceanography*, *37*(4), 309–322. https://doi.org/10.3402/tellusa.v37i4.11675

Maiwa, K., Masumoto, Y., & Yamagata, T. (2010). Characteristics of coastal trapped waves along the southern and eastern coasts of Australia. *Journal of Oceanography*, *66*, 243–258.

Malan, N., Archer, M., Roughan, M., Cetina-Heredia, P., Hemming, M., Rocha, C., et al. (2020). Eddy-Driven Cross-Shelf Transport in the East Australian Current Separation Zone. *Journal of Geophysical Research: Oceans*, *125*(2). http://dx.doi.org/10.1029/2019jc015613

Marchesiello, P., & Middleton, J. H. (2000). Modeling the East Australian Current in the Western Tasman Sea. *Journal of Physical Oceanography*, *30*, 2956–2971.

Mata Mauricio, M., Tomczak, M., Wijffels, S., & Church John, A. (2000). East Australian Current volume transports at 30°S: Estimates from the World Ocean Circulation Experiment hydrographic sections PR11/P6 and the PCM3 current meter array. *Journal of Geophysical Research: Oceans*, *105*(C12), 28509–28526. http://dx.doi.org/10.1029/1999jc000121

Mata Mauricio, M., Wijffels Susan, E., Church John, A., & Tomczak, M. (2006). Eddy shedding and energy conversions in the East Australian Current. *Journal of Geophysical Research*, *111*(C9). http://dx.doi.org/10.1029/2006jc003592

Mellor, G. L., Ezer, T., & Oey, L. Y. (1994). The pressure gradient error conundrum of sigma coordinate ocean models. *Journal of Atmospheric and Oceanic Technology*, *11*, 1126–1134.

Metzger, E., Smedstad, O., Thoppil, P., Hurlburt, H., Cummings, J., Wallcraft, A., et al. (2014). US Navy operational global ocean and Arctic ice prediction systems. *Oceanography*, *27*(3), 32–43.

Moore, A. M., Arango, H. G., & Broquet, G. (2012). Estimates of analysis and forecast error variances derived from the adjoint of 4D-var. *Monthly Weather Review*, *140*(10), 3183–3203. https://doi.org/10.1175/MWR-D-11-00141.1

Moore, A. M., Arango, H. G., Broquet, G., Edwards, C., Veneziani, M., Powell, B. S., et al. (2011). The Regional Ocean Modeling System (ROMS) 4-dimensional variational data assimilation systems: Part III – observation impact and observation sensitivity in the California current system. *Progress in Oceanography*, *91*, 74–94. https://doi.org/10.1016/j.pocean.2011.05.005

Moore, A. M., Arango, H. G., Di Lorenzo, E., Cornuelle, B. D., Miller, A. J., & Neilson, D. J. (2004). A comprehensive ocean prediction and analysis system based on the tangent linear and adjoint of a regional ocean model. *Ocean Modelling*, *7*, 227–258.

Ngodock, H., Souopgui, I., Carrier, M., Smith, S., Osborne, J., & Dâ€™Addezio, J. (2020). An ensemble of perturbed analyses to approximate the analysis error covariance in 4D-var. *Tellus A: Dynamic Meteorology and Oceanography*, *72*(1), 1–12. https://doi.org/10.1080/16000870.2020.1771069

Oke, P. R., Brassington, G. B., Griffin, D. A., & Schiller, A. (2008). The Bluelink ocean data assimilation system (BODAS). *Ocean Modelling*, *21*, 46–70.

Oke, P. R., & Griffin, D. A. (2011). The cold-core eddy and strong upwelling off the coast of New South Wales in early 2007. *Deep Sea Research Part II: Topical Studies in Oceanography*, *58*(5), 574–591. https://doi.org/10.1016/j.dsr2.2010.06.006

Oke, P. R., & Middleton, J. H. (2000). Topographically induced upwelling off eastern Australia. *Journal of Physical Oceanography*, *30*, 512–530.

Oke, P., Sakov, P., Cahill, M. L., Dunn, J. R., Fiedler, R., Griffin, D. A., et al. (2013). Toward a dynamically balanced eddy-resolving ocean reanalysis: BRAN3. *Ocean Modell*, *67*, 52–70.

Oke Peter, R., & Schiller, A. (2007). Impact of Argo, SST, and altimeter data on an eddy-resolving ocean reanalysis. *Geophysical Research Letters*, *34*(19). http://dx.doi.org/10.1029/2007gl031549.

Pasmans, I., Kurapov, A. L., Barth, J. A., Ignatov, A., Kosro, P. M., & Shearman, R. K. (2019). Why gliders appreciate good company: Glider assimilation in the Oregon-Washington coastal ocean 4DVAR system with and without surface observations. *Journal of Geophysical Research: Oceans*, *124*(1), 750–772. https://doi.org/10.1029/2018JC014230

Powell, B. S. (2017). Quantifying how observations inform a numerical reanalysis of Hawaii. *Journal of Geophysical Research: Oceans*, *122*(11), 8427–8444. https://doi.org/10.1002/2017JC012854

Puri, K., Dietachmayer, G., Steinle, P., Dix, M., Rikus, L., Logan, L., et al. (2013). Operational implementation of the ACCESS numerical weather prediction system. *Australian Meteorological and Oceanographic Journal*, *63*, 265–284.

Ribbat, N., Roughan, M., Powell, B., Rao, S., & Kerry, C. G. (2020). Transport variability over the Hawkesbury shelf (31.5-34.5S) driven by the East Australian Current. *PLoS One*, *15*, 622. https://doi.org/10.1371/journal.pone.0241622

Richardson, D. E., Llopiz, J. K., Leaman, K. D., Vertes, P. S., Muller-Karger, F. E., & Cowen, R. K. (2009). Sailfish (*Istiophorus platypterus*) spawning and larval environment in a Florida current frontal eddy. *Progress in Oceanography*, *82*(4), 252–264. https://doi.org/10.1016/j.pocean.2009.07.003

Ridgway, K., & Dunn, J. (2003). Mesoscale structure of the mean East Australian Current system and its relationship with topography. *Progress in Oceanography*, 189–222.

Roughan M., Keating S. R., Schaeffer A., Cetina Heredia P., Rocha C., Griffin D., et al. (2017). A tale of two eddies: The biophysical characteristics of two contrasting cyclonic eddies in the East Australian Current System. *Journal of Geophysical Research: Oceans*, *122*(3), 2494–2518. http://dx.doi.org/10.1002/2016jc012241

Roughan, M., Kerry, C., & McComb, P. (2018). In E. Chassignet, A. Pascual, J. Tintoré, & J. Verron (Eds.), *Shelf and coastal ocean observing and modeling systems: A new frontier in operational oceanography* (pp. 91–116). GODAE OceanView. https://doi.org/10.17125/gov2018.ch04

Roughan, M., & Middleton, J. H. (2002). A comparison of observed upwelling mechanisms off the east coast of Australia. *Continental Shelf Research*, *22*, 2551–2572.

Roughan, M., (2004). On the East Australian Current: Variability, encroachment, and upwelling. *Journal of Geophysical Research*, *109*(C7). http://dx.doi.org/10.1029/2003jc001833

Roughan, M., Schaeffer, A., & Suthers, I. (2014). Sustained Ocean Observing along the coast of Southeastern Australia: NSW-IMOS 2007 -2014. In Y. Lui, H. Kerling, & Weisberg (Eds.), *Coastal ocean observing systems*, (76–98). Elsevier.

Rykova, T., & Oke, P. R. (2015). Recent freshening of the east Australian current and its eddies. *Geophysical Research Letters*, *42*(21), 9369–9378. https://doi.org/10.1002/2015GL066050

Sakov, P., & Sandery, P. A. (2015). Comparison of ENOI and ENKF regional ocean reanalysis systems. *Ocean Modelling*, *89*, 45–60. https://doi.org/10.1016/j.ocemod.2015.02.003

Sandery Paul, A., & Sakov, P. (2017). Ocean forecasting of mesoscale features can deteriorate by increasing model resolution towards the submesoscale. *Nature Communications*, *8*(1). http://dx.doi.org/10.1038/s41467-017-01595-0.

Shchepetkin, A. F., & McWilliams, J. C. (2005). The regional oceanic modeling system (ROMS): A split-explicit, free-surface, topography-following-coordinate oceanic model. *Ocean Modell*, *9*, 347–404.

Shulzitski, K., Sponaugle, S., Hauff, M., Walter, K., D'Alessandro, E. K., & Cowen, R. K. (2015). Close encounters with eddies: Oceanographic features increase growth of larval reef fishes during their journey to the reef. *Biology Letters*, *11*(1), 746. https://doi.org/10.1098/rsbl.2014.0746

Stammer, D. (1997). Global characteristics of ocean variability estimated from regional TOPEX/POSEIDON altimeter measurements. *Journal of Physical Oceanography*, *27*, 1743–1769.

Woodham, R., Brassington Gary, B., Robertson, R., & Alves, O. (2013). Propagation characteristics of coastally trapped waves on the Australian Continental Shelf. *Journal of Geophysical Research: Oceans*, *118*(9), 4461–4473. http://dx.doi.org/10.1002/jgrc.20317

Zavala-Garay, J., Wilkin, J. L., & Arango, H. G. (2012). Predictability of mesoscale variability in the East Australian Current given strong-constraint data assimilation. *Journal of Physical Oceanography*, *42*, 1402–1420.